CHAPTER 6

RESULTS AND DISCUSSION (PART III):

Lead Zirconate Titanate-Lead Magnesium Niobate (PZT-PMN) Ceramics

In the previous two chapters the details of PZT and PMN powders have been fully explained both in terms of preparation and characterizations. In this chapter, these powders are used as the starting materials for fabricating the ceramics in the *x*PZT-(1-*x*)PMN system. It is known that the density and the yield of perovskite phase are the most important factors for ensuring good dielectric respond of the materials. Thus, the effects of sintering conditions on densification, microstructure and dielectric properties are primary explored. Then, necessary characterization techniques were carried out on the selected samples and the results are discussed relating to their composition, microstructure and dielectric properties.

6.1 Phase Analysis

Compositions in the pseudo-binary system *x*PZT-(1-*x*)PMN (*x* = 0.0, 0.1, 0.3, 0.5, 0.7, 0.9 and 1.0) have been fabricated from PZT and PMN precursor powders, employing a combination of a mixed oxide synthetic route and normal sintering methods. Concentration of perovskite and pyrochlore phases and optimum sintering temperatures of the entire compositional range and given in Table 6.1.

Table 6.1 Phase formation of *x*PZT-(1-*x*)PMN ceramics sintered at various temperatures.

Sintering temperature	*x* = 0.1		*x* = 0.3		*x* = 0.5		*x* = 0.7		*x* = 0.9	
	Perovskite	Pyrochlore	Perovskite	Pyrochlore	Perovskite	Pyrochlore	Perovskite	Pyrochlore	Perovskite	Pyrochlore
(^{o}C)	(wt%)	(wt%)	(wt%)	(wt%)	(wt%)	(wt%)	(wt%)	(wt%)	(wt%)	(wt%)
1100	-	-	-	-	100	0	100	0	100	0
1150	94.88	5.12	-	-	100	0	100	0	100	0
1200	97.68	2.32	97.35	2.65	100	0	100	0	100	0
1225	97.06	2.94	97.67	2.33	100	0	100	0	100	0
1250	95.48	4.52	100	0	100	0	100	0	100	0
1275	94.88	5.12	99.31	0.69	100	0	100	0	100	0
1290	96.10	3.90	98.35	1.65	100	0	100	0	100	0
1320	-	-	98.00	2.00	100	0	100	0	100	0

X-ray diffraction patterns of *x*PZT-(1-*x*)PMN ceramics sintered at various temperatures with maximum perovskite phase of bulk ceramics are given in Fig. 6.1, indicating the formation of both perovskite and pyrochlore phases in each composition. In this study, it is evident that except at $x = 0.1$, complete crystalline solid solution of perovskite structure were formed throughout the whole compositional range of *x*PZT-(1-*x*)PMN system. Although, the effectiveness of the B-site precursor method in suppression of the pyrochlore formation during perovskite development in lead-based perovskite systems has been reported by several researchers.[21, 126, 137-140] However, in the work reported here, small amounts of second phase (*) correlating with a pyrochlore phase of $Pb_{1.83}Mg_{0.29}Nb_{1.71}O_{6.39}$ (JCPDS file no. 33-769)[126] could be detected by XRD in the composition of $x = 0.1$. This could be attributed to its poor homogeneity due to the limitation of a mixed oxide processing especially the ball-milling and also volatility of PbO at high firing temperature.

For $x = 0.0$ (pure PMN), the X-ray diffraction pattern shows only single (200) peak, confirming its (pseudo)cubic symmetry at room temperature, in good agreement with those observed by other workers.[139, 141] When the *x* value increases to 0.3, the broadened peaks especially at $2\theta \sim 44.5^{o}$-45^{o} show that the distortion of the (pseudo)cubic lattice is enlarged. At $x = 0.5$, the structure transforms to tetragonal phase because of lattice deformation, which are characterizated by (002)/(200) peak splitting around 2θ of 44^{o}-45^{o} (Fig. 6.2). By increasing the PZT content, the intensity ratios of the (002)/(200) peaks tend to increase until at $x = 1.0$, where the peaks matched that of piezoelectric PZT. The variation of these doublet-diffraction lines as a function of PZT content could be explained by microscopic compositional fluctuations occurring in these perovskite materials, which cannot provide a real

homogeneity in the solid solutions, and also by the different stresses induced in the particles, which determined the existence of tetragonal ferroelectric phases.[142]

The lattice parameters of the perovskite phase were calculated from the XRD data and plotted as a function of PZT content (Fig. 6.3), along with tetragonality factor (or axial ratio of c/a) and average lattice parameters of $(a^2c)^{1/3}$. The parameters of (pseudo)cubic PMN ($x = 0.0$) and tetragonal PZT ($x = 1.0$) are 0.4046 nm, and a = 0.4033 and c = 0.4132 nm, respectively, which are in consistent to reported data (JCPDS file nos. 81-861 and 50-376).[132, 143] The results of the cell refinement show that all the PZT-PMN compositions having PZT content in the range between $x = 0.0$ and $x = 0.4$ have single phase (pseudo)cubic symmetry, with the cell parameters dependent on the PZT content. At $x = 0.5$, however, peaks splitting are detected in Fig. 3, with a = 0.4050 and c = 0.4060 nm, and c/a = 1.0024. From the crystallographic analyses, therefore, the phase boundary between the (pseudo)cubic and tetragonal symmetries seems to be located at $x = 0.3$-0.5. However, this real composition boundary could not be determined under the present experimental limit of accuracy. The possible ranges of compositions for further studies are $0.3 < x < 0.5$. High resolution XRD analysis is necessary to detect the possible superposition of phases and to restrict the range of compositions for a better characterization of the PZT-PMN compositions in the range of structural change.

With further increases in x, the a-axis shrunk while the c-axis expanded continuously at approximately similar rates. Consequently, the values of $(a^2c)^{1/3}$ increased slowly, while the axial ratios of c/a increased rapidly to 1.0245. By comparing the B-site cation sizes of PMN and PZT[137], the continuous increase in the average lattice parameter (from 0.4046 nm at $x = 0.0$ to 0.4098 nm at $x = 1.0$) can be

well understood, which supports the formation of complete crystalline solutions of a perovskite structure. In this experiment, the lattice parameters calculated from the diffraction data indicate that the *c*/*a* axial ratio increases as the PZT content (*x*) increases.

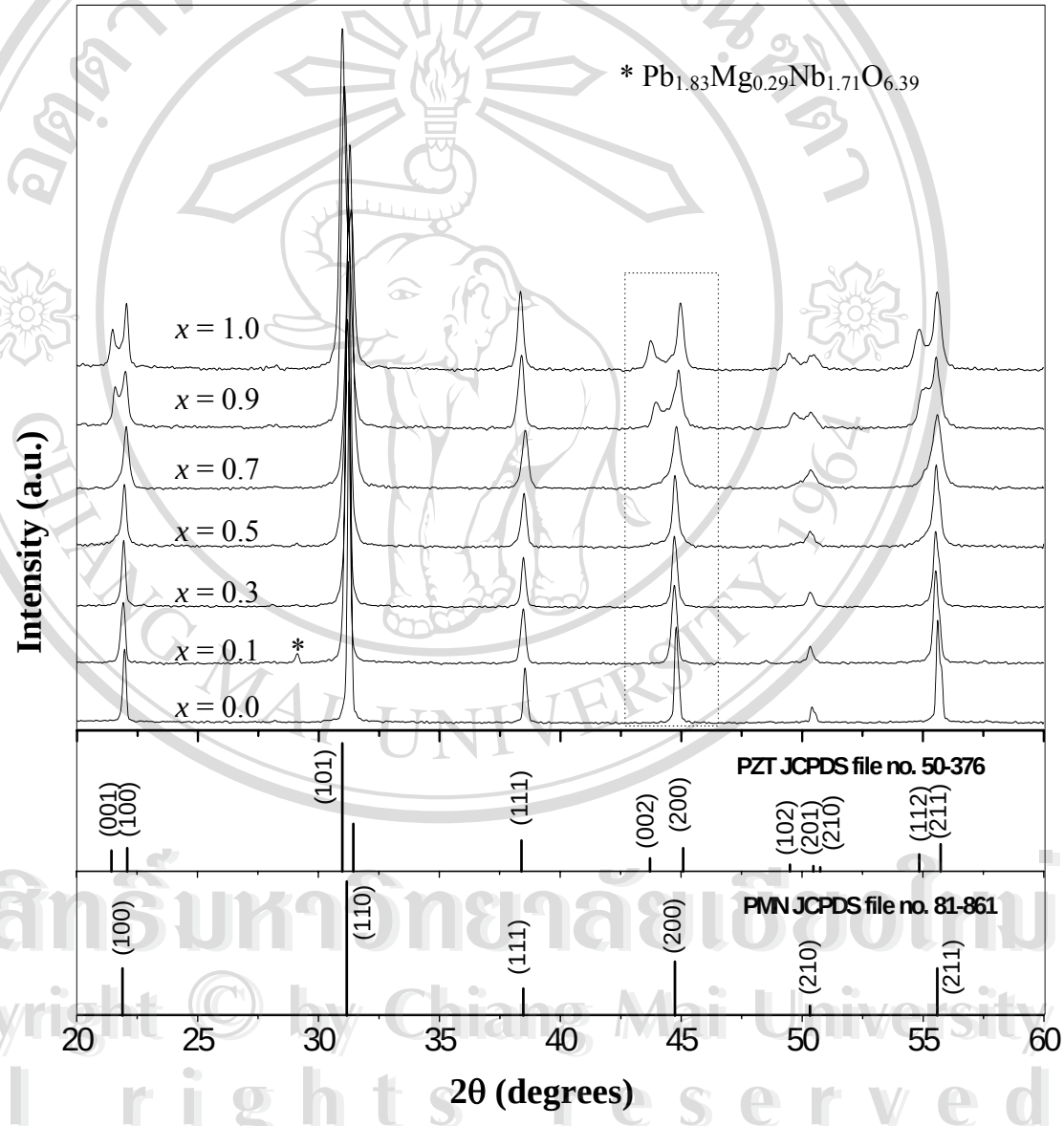

Fig. 6.1 XRD patterns of the *x*PZT-(1-*x*)PMN ceramics sintered at their optimum conditions.

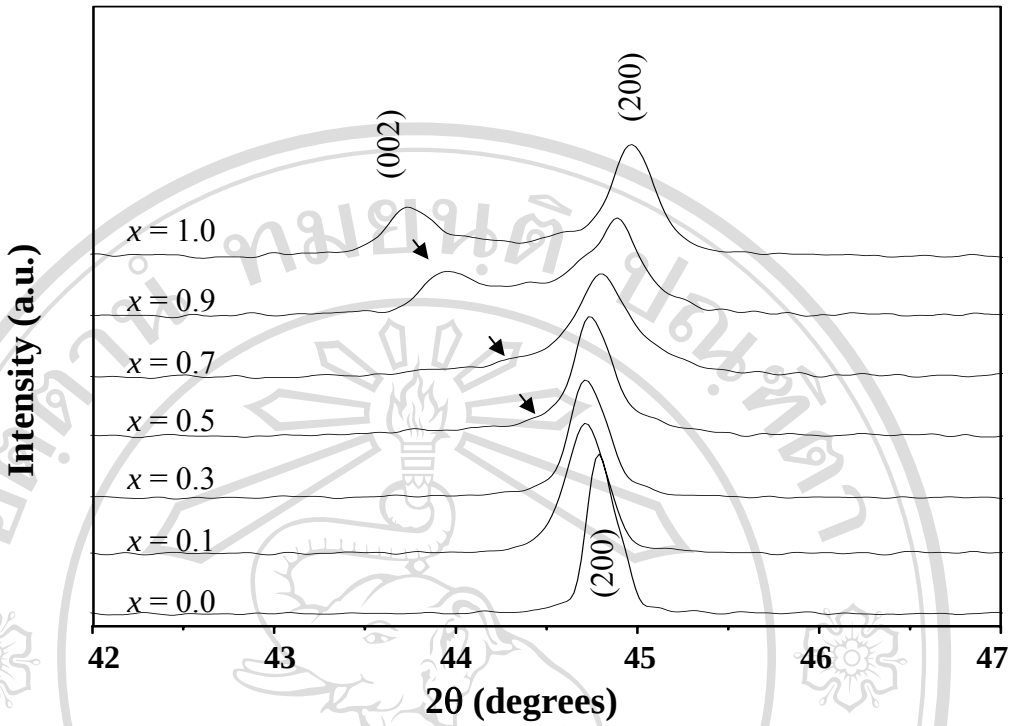

Fig. 6.2 Selected region of the diffraction patterns for *x*PZT-(1-*x*)PMN ceramics.

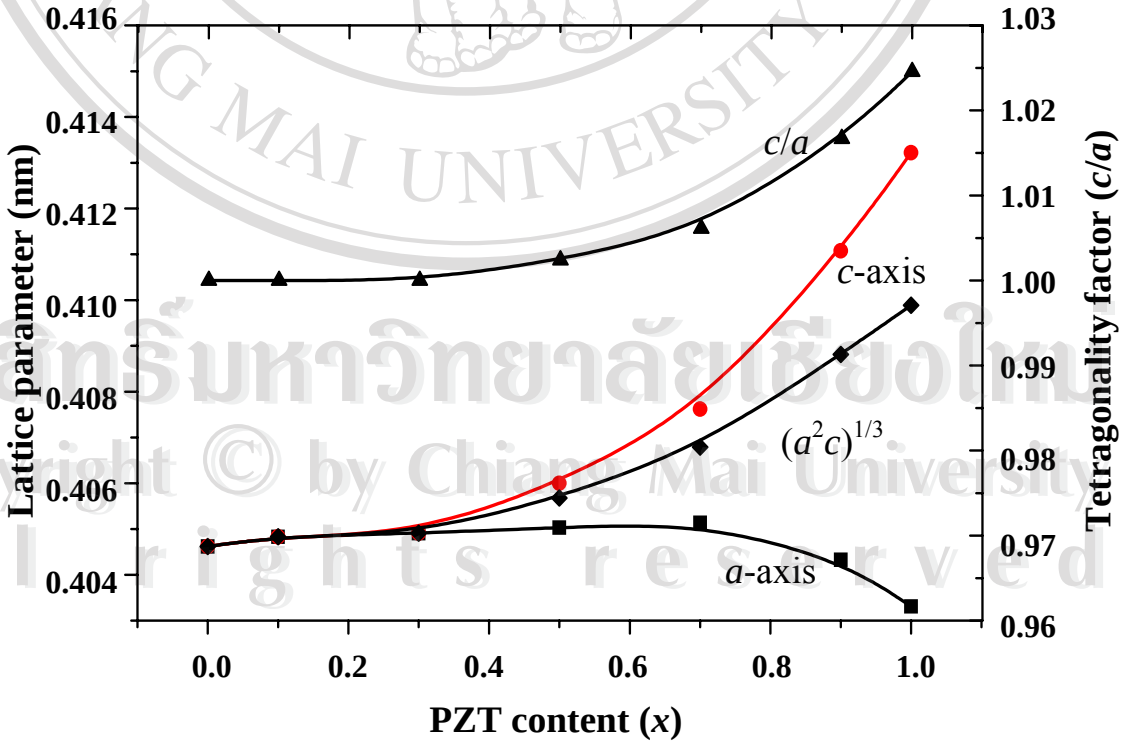

Fig. 6.3 Variation of cell parameters in the *x*PZT-(1-*x*)PMN system.

X-ray diffraction patterns of *x*PZT-(1-*x*)PMN ceramics sintered at various temperatures are given in Figs. 6.4-6.9, indicating the formation of both perovskite and pyrochlore phases in each composition. The strongest reflections in the majority of the XRD patterns indicated the formation of perovskite phase. In this study, it is evident that complete crystalline solid solution of perovskite structure were formed throughout the whole selected sintering temperature range (1150-1290 ^{o}C) in samples at compositions of *x* between 0.5 to 0.9. Whilst for composition with PZT content of *x* = 0.3, single phase of perovskite structure was found only at 1225 ^{o}C. For other cases, small amounts of second phase could be detected by XRD, with additional reflections (marked by *), correlating with a pyrochlore phase of composition $Pb_{1.83}Mg_{0.29}Nb_{1.71}O_{6.39}$ (JCPDS file no. 33-769) commonly found in the fabrication of PMN-based materials.[120] This could be attribute to their poor homogeneity due to the limitation of a mixed oxide processing and also volatility of PbO at high firing temperatures. In order to evaluate the concentration of perovskite and pyrochlore phases, equation (3.5) was applied to these XRD patterns and the results are given in Table 6.1.

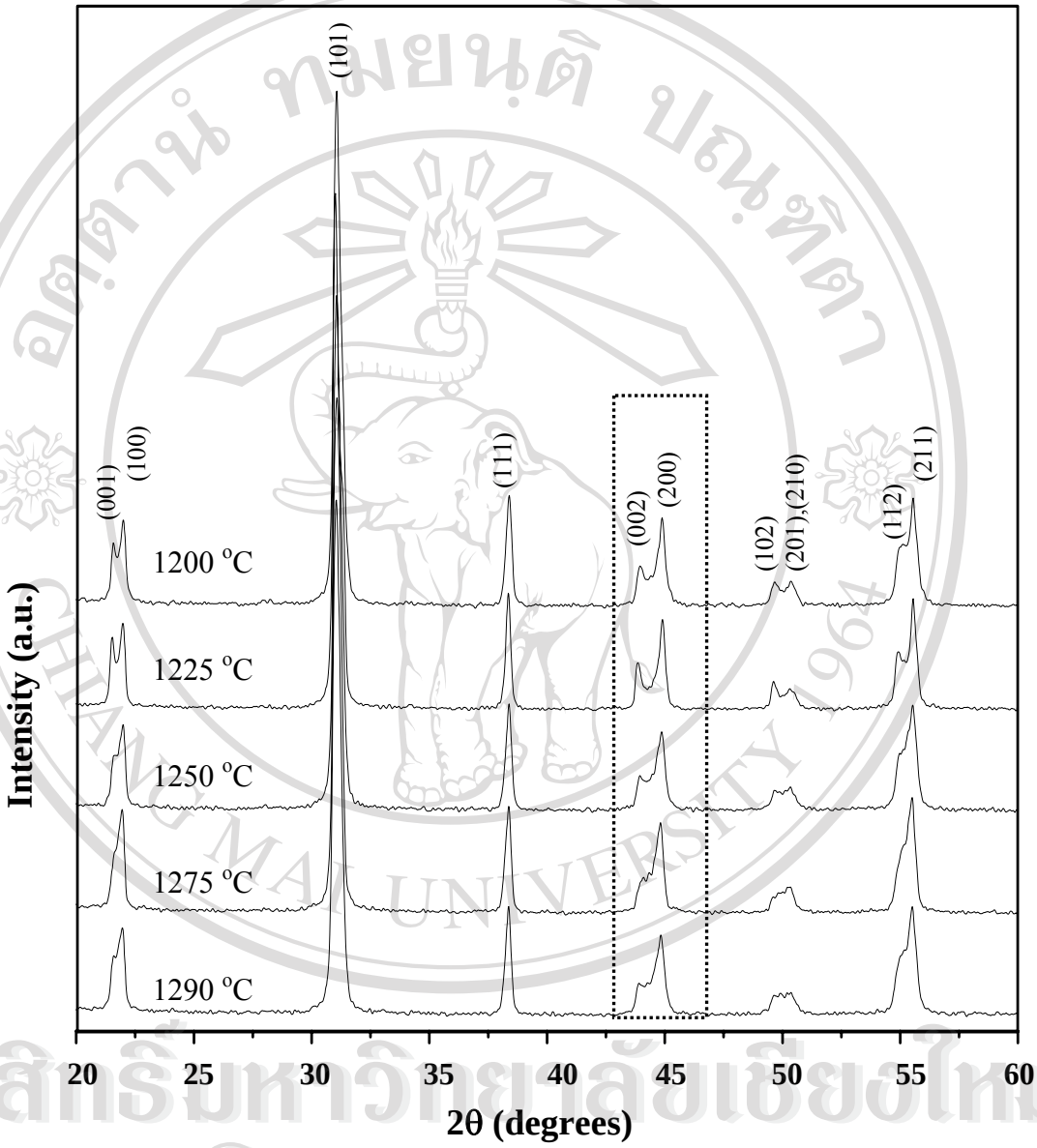

Fig. 6.4 XRD patterns of 0.9PZT-0.1PMN ceramics sintered at various temperatures for 4 h with heating/cooling rates of 10 °C/min.

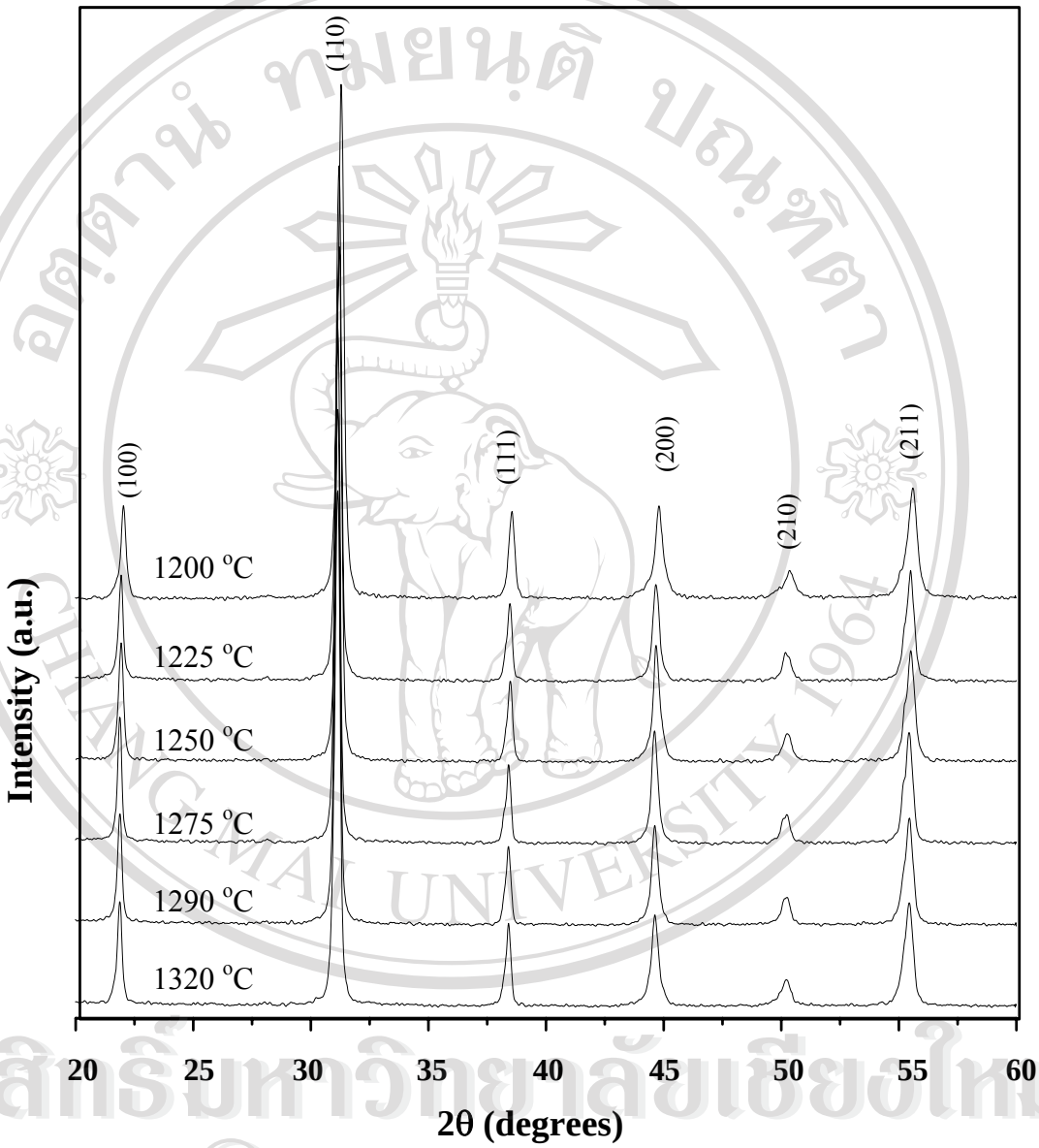

Fig. 6.5 XRD patterns of 0.7PZT-0.3PMN ceramics sintered at various temperatures for 4 h with heating/cooling rates of 10 °C/min.

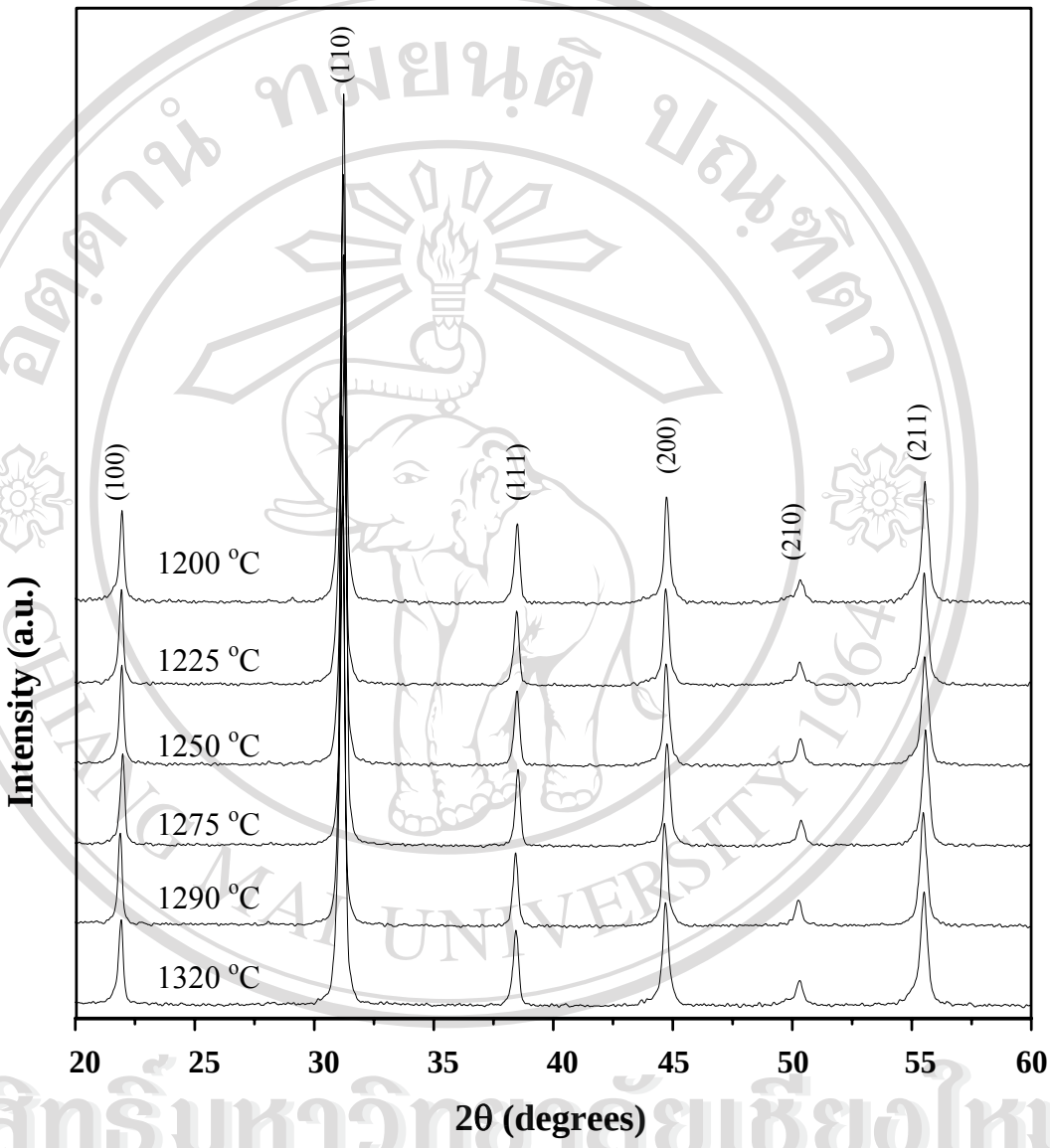

Fig. 6.6 XRD patterns of 0.5PZT-0.5PMN ceramics sintered at various temperatures for 4 h with heating/cooling rates of 10 °C/min.

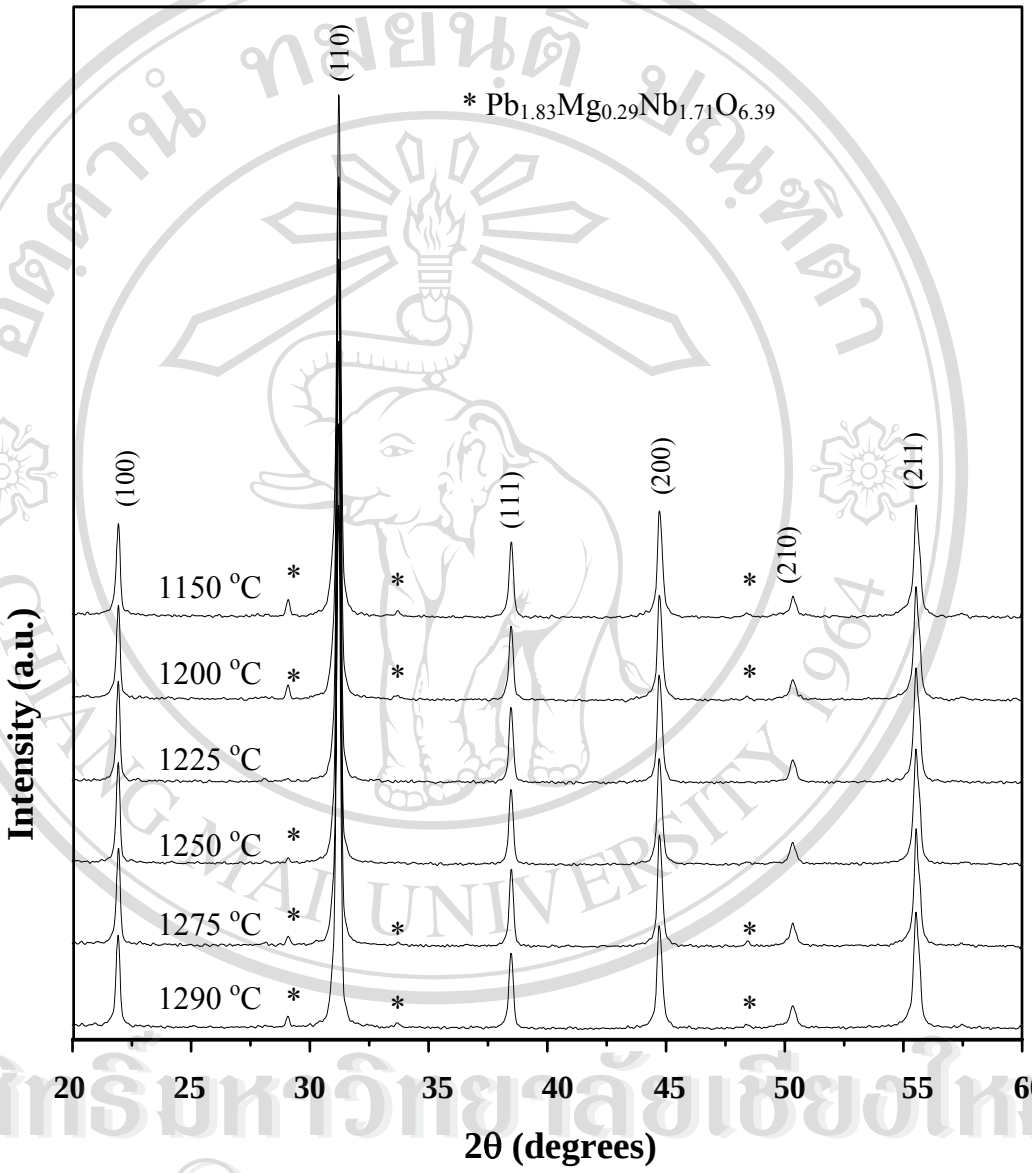

Fig. 6.7 XRD patterns of 0.3PZT-0.7PMN ceramics sintered at various temperatures for 4 h with heating/cooling rates of 10 °C/min.

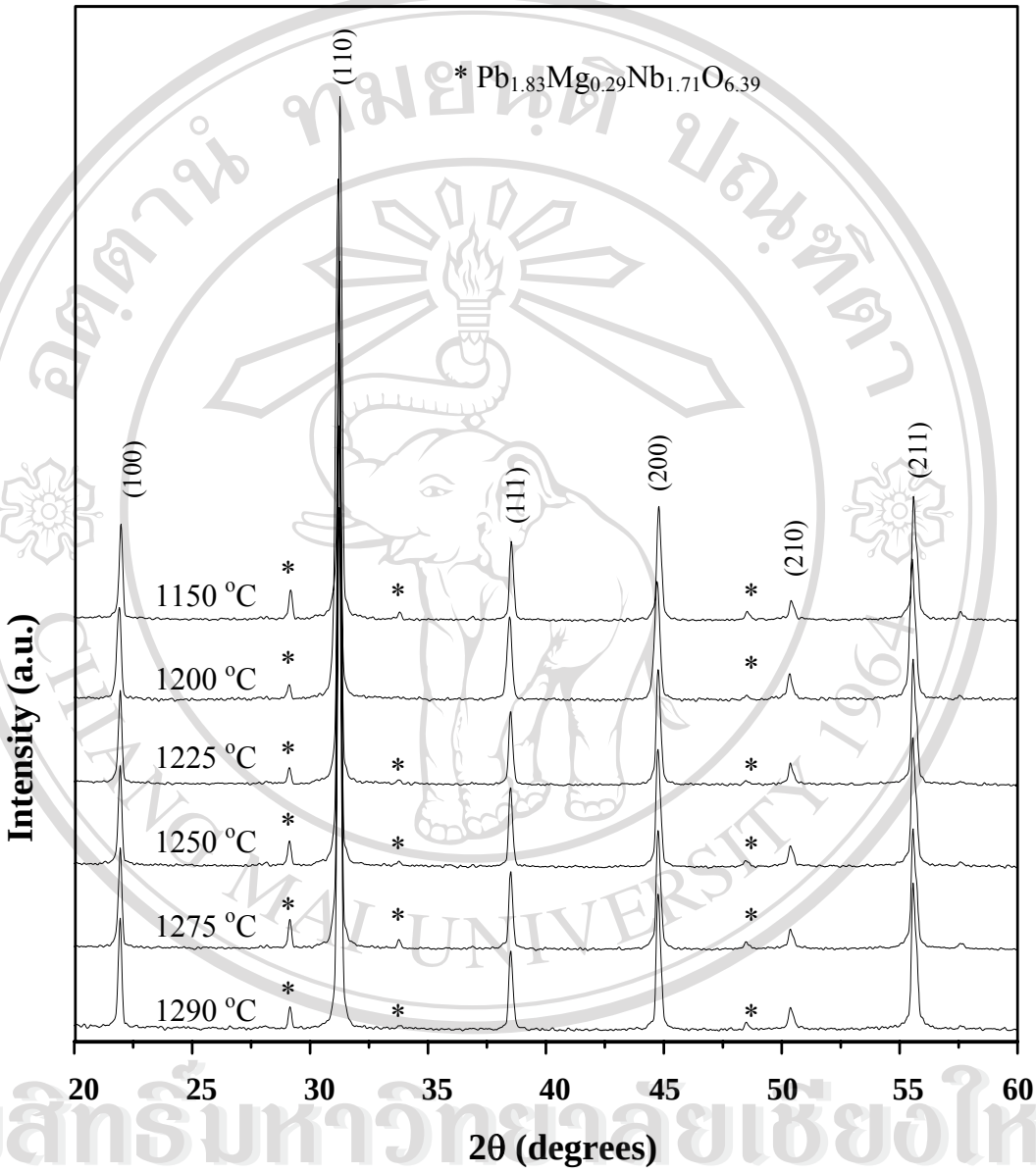

Fig. 6.8 XRD patterns of 0.1PZT-0.9PMN ceramics sintered at various temperatures for 4 h with heating/cooling rates of 10 °C/min.

6.2 Densification and Microstructural Analysis

Calculated relative densities, shrinkage and optimum sintering conditions of the entire compositional range are given in Table 6.2. Density variations of all compositions exhibit the same tendency, as shown in Fig. 6.9. At sintering temperature 1100-1200 ^{o}C, gradually increase of the densities are observed corresponding to the larger shrinkage observed in this temperature range. For the higher sintering temperature, densities are only slightly increased. After the sintering temperature exceed 1300 ^{o}C, decreasing of densities as the same as linear shrinkage are clearly seen. However, densification of sample with x = 0.7 is different from the others as it gives a comparable density only when sintered at above 1250 ^{o}C. These results may be associated with solubility behaviour of both constituents. For the example of xPZT-(1-x)PMN when x = 0.1 and 0.3, samples that contain PMN in a larger proportion, PZT can be dissolved more easily at the lower temperature. In the same way for 0.9PZT-0.1PMN, less proportion of PMN was dissolved into PZT. Distinctive densification behaviour found in the latter sample, 0.7PZT-0.3PMN. This may be due to the solubility limit of both PZT and PMN because they present in a closer proportion. This is probably the reason why samples form a solid solution in a higher temperature range as clearly seen in Figs. 6.9 (a) and (b).

In this work, it is observed that the maximum densification value can be obtained from the samples sintered at 1225 ^{o}C, only in sample composition of x = 0.1, at 1275 ^{o}C, in samples composition of 0.3, 0.5 and 0.9 and at 1290 ^{o}C, in sample composition of 0.7. The observed fall-off in density at 1320 ^{o}C is probably due to PbO volatilization impeding the sintering process and the lower density of the pyrochlore phase, in good agreement with other workers.[104, 144, 145]

In Table 6.2, the results of densities and shrinkage are summarised as a function of sintering temperature. It can be seen that both density and shrinkage are going to a maximum value at certain sintering temperatures. This characteristic indicates a normal solid-state sintering mechanism. According to the results, it can be summarized that except $x = 0.7$, density and shrinkage of all compositions change with sintering temperature in a similar fashion and consistent with those found in typical lead-based perovskite ceramics.[146-149]

Table 6.2 Density* and shrinkage** of *x*PZT-(1-*x*)PMN ceramics sintered at various temperatures.

Sintering temperature (^oC)	$x = 0.1$		$x = 0.3$		$x = 0.5$		$x = 0.7$		$x = 0.9$	
	Density (g/cm^3)	Shrinkage (%)	Density (g/cm^3)	Shrinkage (%)	Density (g/cm^3)	Shrinkage (%)	Density (g/cm^3)	Shrinkage (%)	Density (g/cm^3)	Shrinkage (%)
1100	6.02	4.27	5.83	3.33	-	-	-	-	5.40	0.87
1150	7.60	11.76	7.04	8.83	-	-	-	-	7.02	7.31
1200	7.87	**13.84**	7.68	12.68	7.26	11.19	6.21	7.94	7.42	9.71
1225	**7.90**	13.57	7.73	13.31	7.19	12.13	6.47	8.74	7.40	11.09
1250	7.83	13.43	7.86	13.41	7.33	**13.18**	7.33	11.65	7.52	**11.26**
1275	7.78	13.23	**7.91**	**13.59**	**7.84**	13.10	7.78	**12.91**	**7.56**	10.59
1290	7.73	13.61	7.85	12.95	7.84	13.03	**7.87**	12.57	7.51	9.91
1320	7.51	12.25	7.67	11.45	7.76	11.23	7.60	10.69	7.30	8.05

* The estimated precision of the density is ± 0.2% ** The estimated precision of the shrinkage is ± 0.2%

- : data not available due to high porous samples with poor sintered shape.

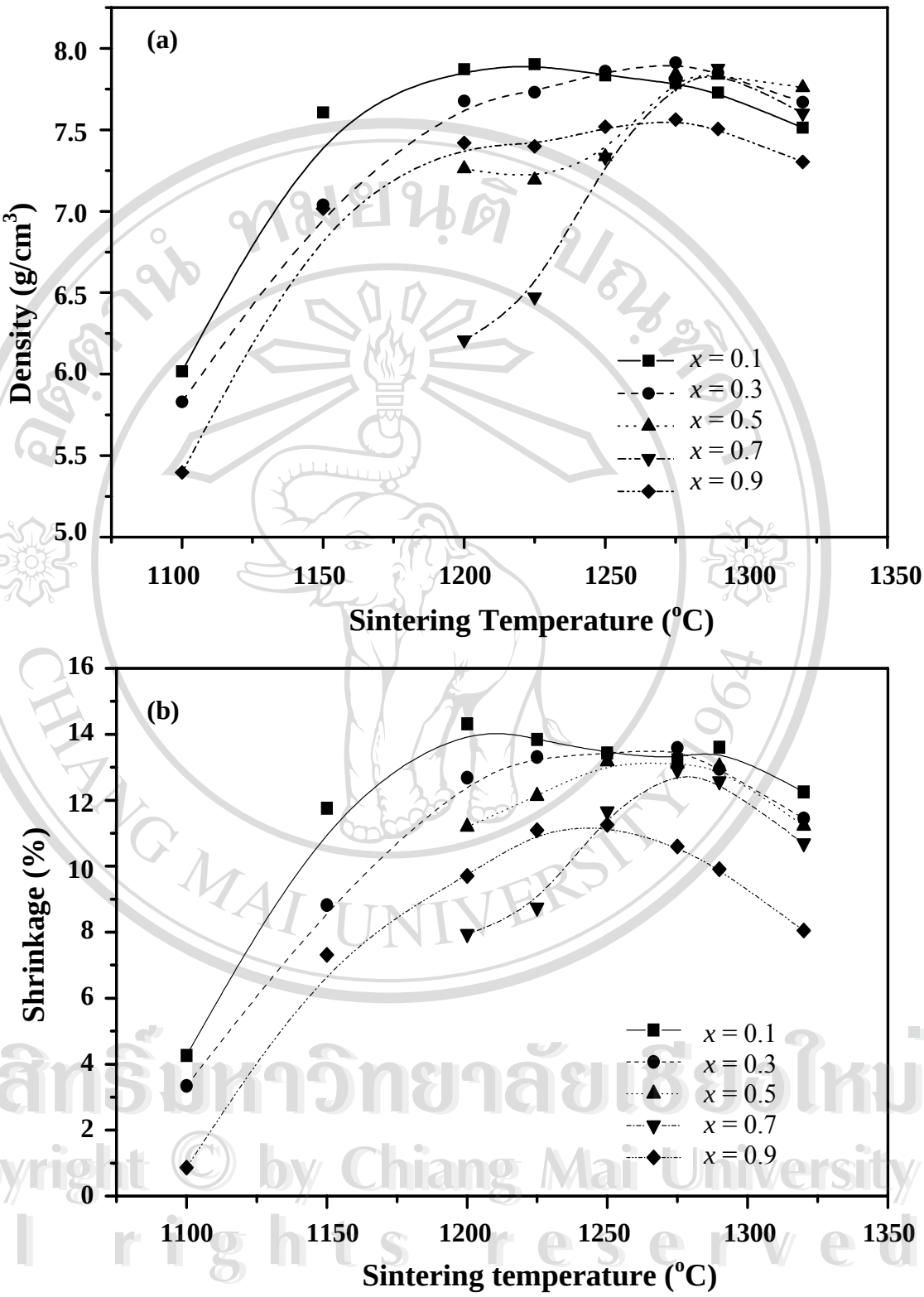

Fig. 6.9 Dependence of (a) bulk densities and (b) shrinkage on sintering temperature for *x*PZT-(1-*x*)PMN ceramics.

SEM-micrographs of as fired surfaces of all compositions are shown as a function of sintering temperature in Figs. 6.10-6.14. In general, irregular microstructural characteristics were observed in these samples, i.e. non spherical, no uniform grain size and shape. Abnormal grain growth was observed almost at high sintering temperatures in all compositions. By applying the linear intercept method to these SEM micrographs, mean grain sizes of about 1.6-12.0 μm were estimated for these samples, as given in Table 6.3. It should be seen as a rough approximation since the micrographs exhibit only 2 dimensional images of the unpolished samples. It is seen that the grain size varies significantly as a function of chemical compositions and sintering temperatures. The results indicate that grain size tend to increase with sintering temperature, in agreement with other researchers.[150-152] The microstructure become denser as the sintering temperature increase up to 1290 ^{o}C, as indicated by the grain packing and increases in grain boundary thickness. It should be noted that some phases appear as insertion randomly distribute within matrix of the major phase, as shown in Fig. 6.15. This observation agrees well with the XRD results. The appearance of this pyrochlore phase can be attributed to volatilization of PbO from perovskite matrix, in consistent with Koval et al.[153]

Fig. 6.10 shows SEM micrographs of 0.9PZT-0.1PMN ceramics sintered at various temperatures for 4 h. It is seen that the grain size and shape varies significantly as a function of sintering temperatures. The appearance of some white phases (~0.34 μm) especially at higher temperatures could be attributed to the limitation of a ball-milling and/or volatilization of PbO from perovskite matrix, in consistent with other work. [126]

It is interesting to noted that the 0.9PZT-0.1PMN ceramics sintered above 1250 ^{o}C exhibit totally different microstructures. The grain size increases drastically from about 1.0-3.75 μm for ceramics sintered at 1200 ^{o}C to 2.62-10.25 μm for samples sintered at 1275 ^{o}C, although starting from compacted powders with similar granulometry. For the 0.7PZT-0.3PMN ceramics, similar trend of microstructural development upon increasing sintering temperature was also observed as shown in Fig. 6.11. It is evident that highly densed grain-packing with thinner grain boundaries is found in ceramics sintered above 1275 ^{o}C (see Figs. 6.11(d) & (e)). By increasing PMN content from 0.5 to 0.9 mol%, uniformly sized grains with a high degree of grain close-packing and rounded (low degree of angularity) microstructural characteristics were observed. Almost no abnormal grain growth was found, although some small particles with diameter about 0.34 μm were detected at the grain boundaries and triple junctions of these samples. Similar microstructural characteristics were also reported by Koval et al.[153] and Yoon et al.[154]

For 0.5PZT-0.5PMN ceramics, their microstructures are shown in Fig. 6.12. The average grain size increased with increasing sintering temperature up to 1290 ^{o}C. Increasing temperature does not promote a larger grain size but rather induces occurrence of porosity (Fig. 6.12 (d)). Microstructure of 0.5PZT-0.5PMN ceramics are similar to that one shown by Koval et al.[153] Increasing of PMN concentration in 0.3PZT-0.7PMN and 0.1PZT-0.9PMN ceramics, the grain growth with increasing sintering temperature are observed. The grain shape of these particular samples display nearly spherical shape as found in pure PMN ceramics.

It can be seen that the samples contained higher PZT content tend to show a larger average grain size compared with one that introduced more PMN content.

These results reveal that with increasing PMN content, the grain size does not change significantly which consistent with the report of Koval et al.[73] Also, the microstructure become apparently more uniform with small grain as the amount of PMN increased. The same results has been also reported for the sample prepared using sol-gel method by Yoon et al.[72] Incresing of PMN content has been also reported to reduce the rate of grain growth.[153] But, such a reduction can not be observed here because there is no enough evidence. The irregular grain shape observed in the 0.9PZT-0.1PMN sintered at 1275 and 1290 ^{o}C (Figs. 6.10 (e) & (f)) were probably due to loss of some lead content which is seen as appearance of porosity. The similar observation was also found in the pure PZT ceramics sintered with a slow heating/cooling rates which loss of lead content can undergo as a result of longer sintering duration. Fig. 6.15 shows SEM micrograph taken from polished surface of 0.1PZT-0.9PMN ceramics sintered at 1275 ^{o}C. The microstructure of this sample is observed as coexistence of the secondary phases which are seen as darker grains dispersed in a matrix of lighter grains. The XRD results of this particular composition have suggested that the secondary phase was strongly present even sintering at different conditions. Thus, the darker grains seen in this SEM micrograph may correspond to that revealed by XRD as the pyrochlore phase with composition $Pb_{1.83}Mg_{0.29}Nb_{1.71}O_{6.39}$.

For each sample, increasing of grain size as a result of increasing of sintering temperature have provided denser matrix as seen by increasing of the density (shown in the previous section). However, at the higher sintering temperature, abnormal grain growth which is seen as irregular grain shape and size also effect to a decreasing of the density. Most of these effects are believed to be due to the consequence of PbO

content loss. Increasing sintering temperature of 0.7PZT-0.3PMN sample, rate of grain growth seem to be higher than other samples and give a higher degree of densification (Fig. 6.9).

Table 6.3 Grain size* of *x*PZT-(1-*x*)PMN ceramics sintered at various temperatures.

Sintering temperature (°C)	*x* = 0.1		*x* = 0.3		*x* = 0.5		*x* = 0.7		*x* = 0.9	
	Average (μm)	Range (μm)	Average (μm)	Range (μm)	Average (μm)	Range (μm)	Average (μm)	Range (μm)	Average (μm)	Range (μm)
1150	1.60	0.37-2.46	1.74	0.54-2.07	-	-	-	-	-	-
1200	2.69	1.16-5.58	2.00	0.50-3.04	-	-	2.63	0.47-5.95	2.25	1.0-3.75
1225	**3.80**	**1.16-6.28**	2.78	0.66-3.22	-	-	3.94	0.96-8.19	5.65	1.71-7.23
1250	5.32	1.82-8.41	3.46	0.98-6.91	2.27	0.97-6.83	3.30	0.75-5.50	6.61	1.81-9.73
1275	6.90	1.80-11.71	**5.61**	**1.75-8.25**	**4.58**	**0.96-6.74**	11.37	1.96-16.52	**6.67**	**2.62-10.25**
1290	-	-	-	-	5.33	1.22-7.09	**12.09**	**2.22-20.0**	-	-

* These data were taken by estimating from SEM micrographs with the estimated precision of ± 0.10 μm.

-: data not available due to very high porous ceramic was abtained.

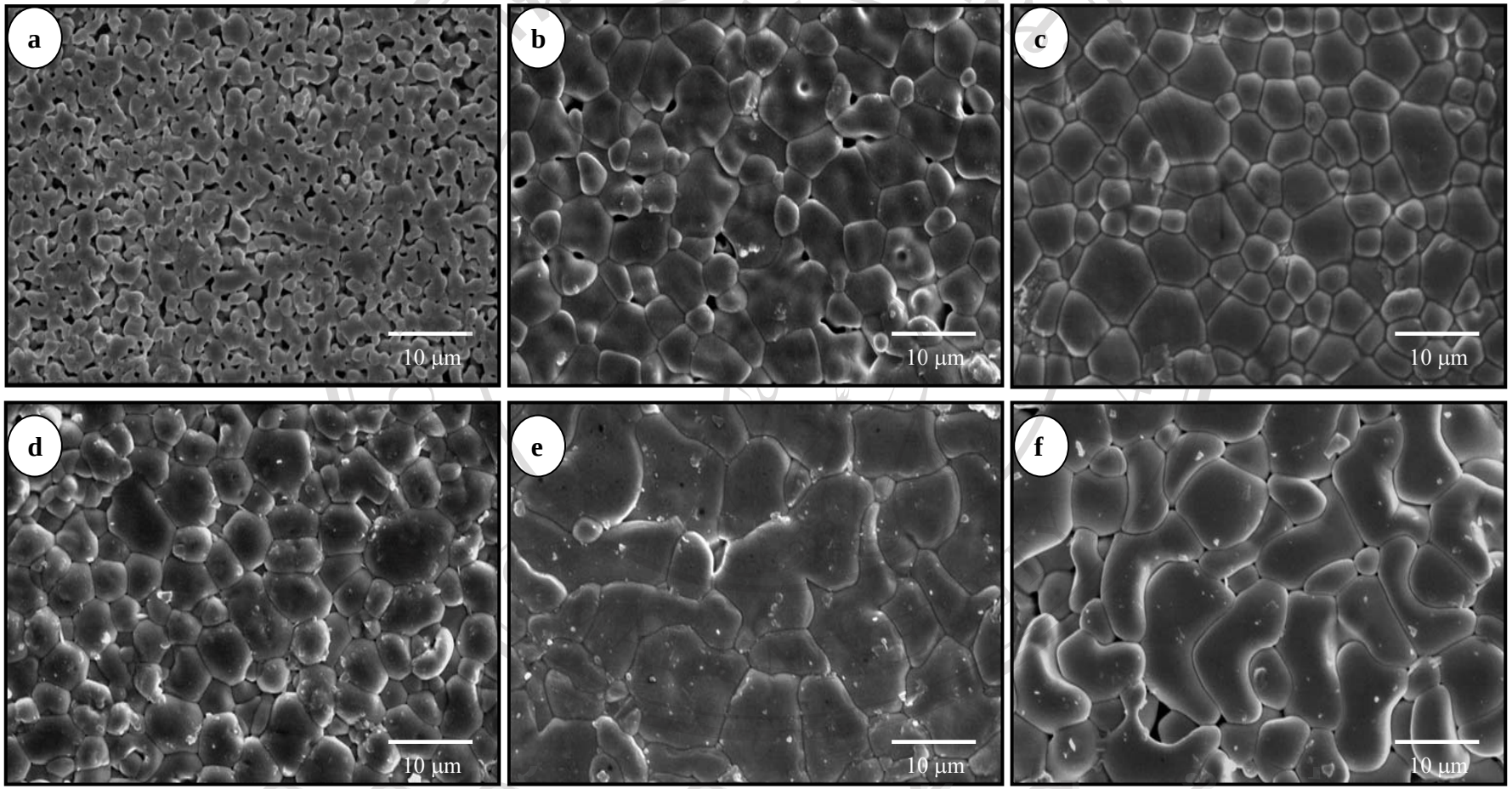

Fig. 6.10 SEM micrographs of 0.9PZT-0.1PMN ceramics sintered for 4 h at (a) 1150 ^{o}C, (b) 1200 ^{o}C, (c) 1225 ^{o}C, (d) 1250 ^{o}C, (e) 1275 ^{o}C and (f) 1290 ^{o}C.

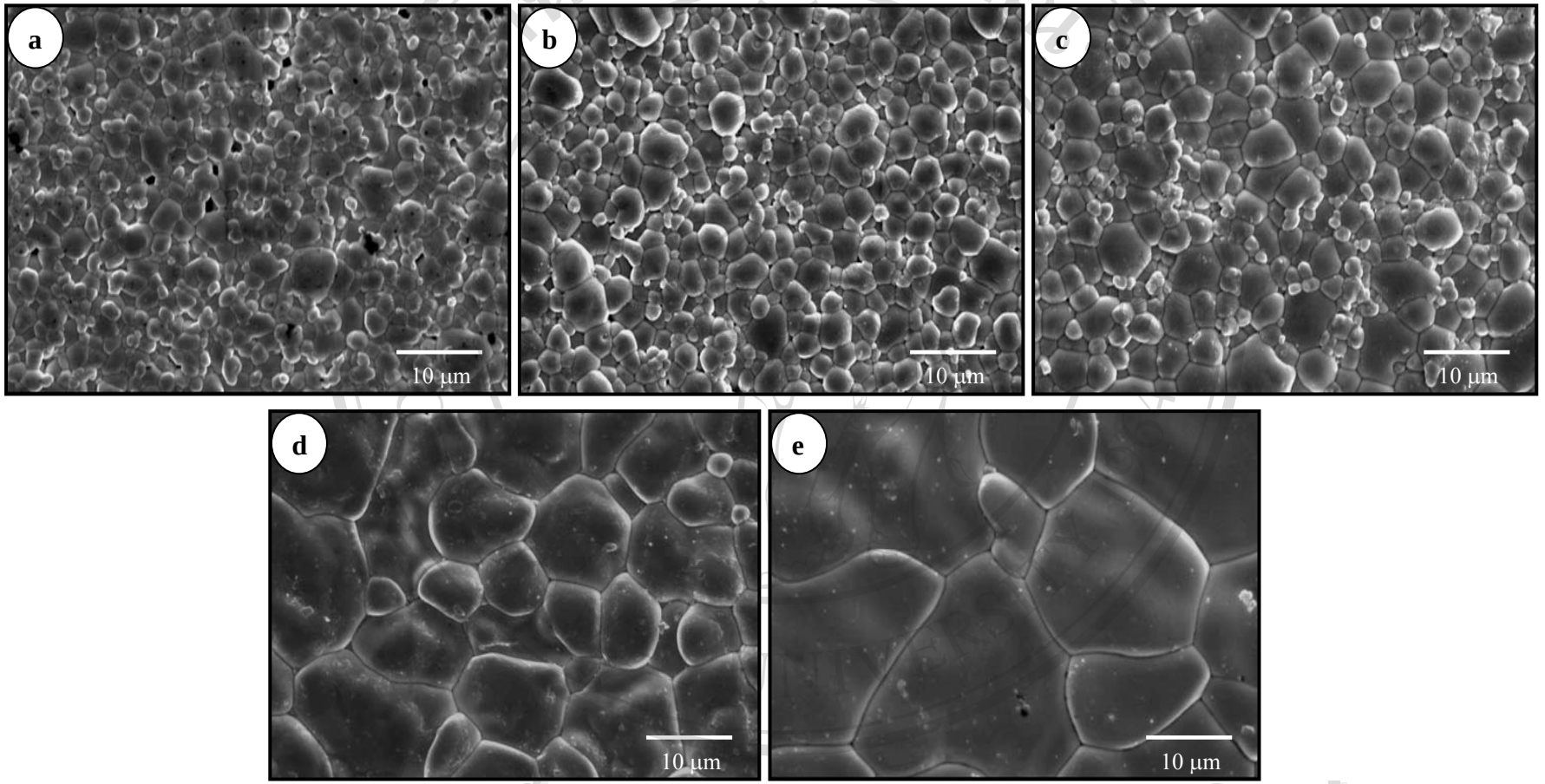

Fig. 6.11 SEM micrographs of the 0.7PZT-0.3PMN ceramics sintered for 4 h at (a) 1225 ^{o}C, (b) 1250 ^{o}C, (c) 1275 ^{o}C, (d) 1290 ^{o}C and (e)1320 ^{o}C.

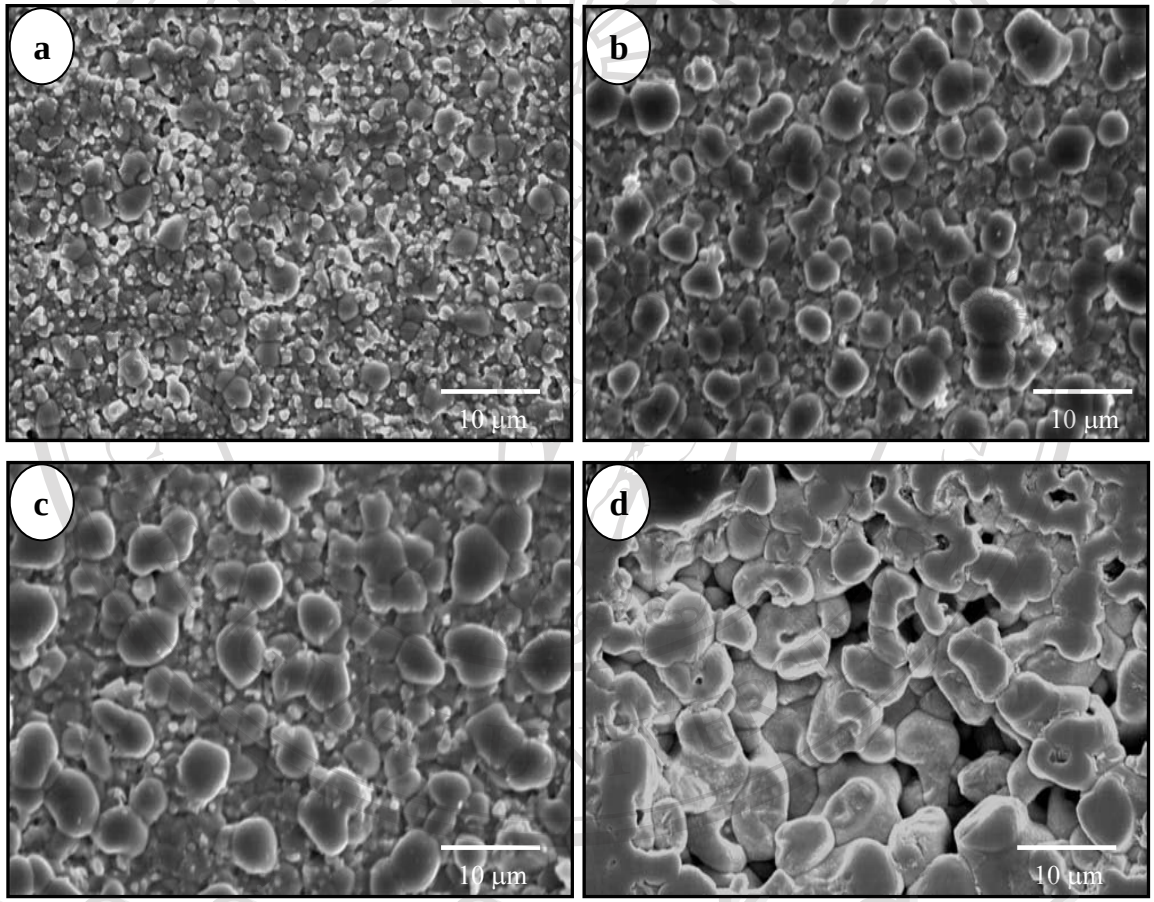

Fig. 6.12 SEM micrographs of the 0.5PZT-0.5PMN ceramics sintered for 4 h at (a) 1250 ^{o}C, (b) 1275 ^{o}C, (c) 1290 ^{o}C and (d) 1320 ^{o}C.

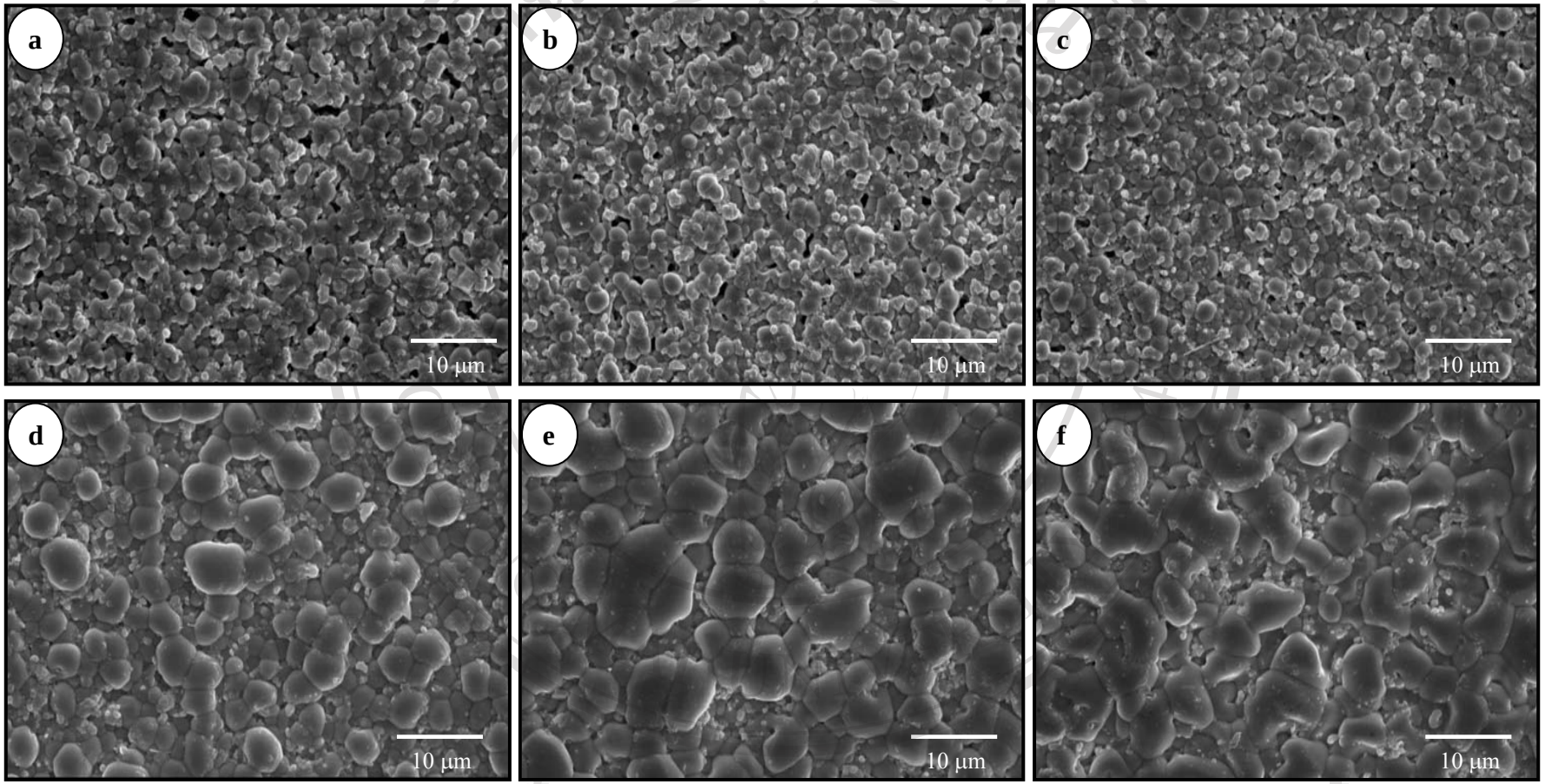

Fig. 6.13 SEM micrographs of the 0.3PZT-0.7PMN ceramics sintered for 4 h at (a) 1150 ^{o}C, (b) 1200 ^{o}C, (c) 1225 ^{o}C, (d) 1250 ^{o}C, (e) 1275 ^{o}C and (f) 1290 ^{o}C.

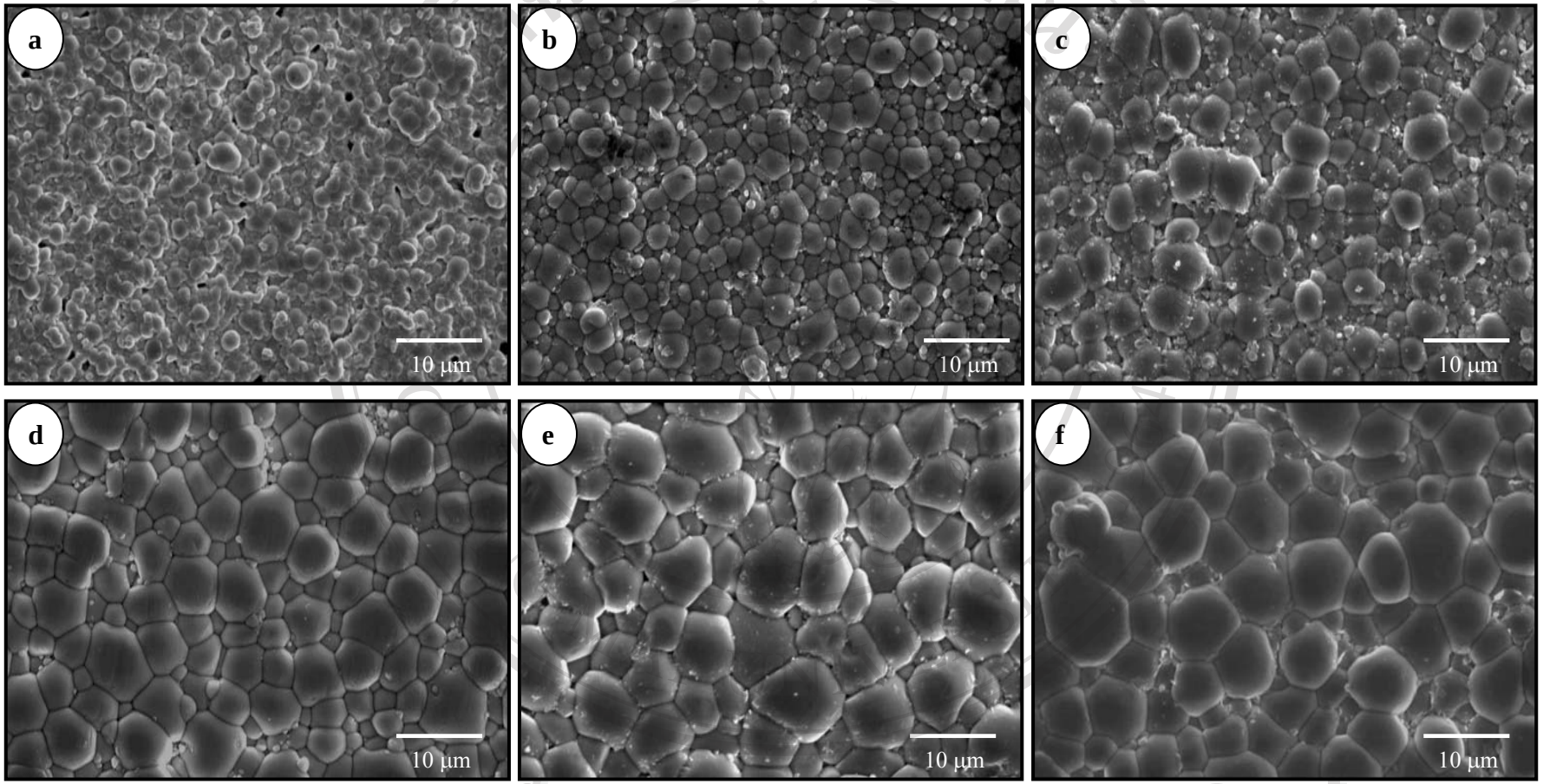

Fig. 6.14 SEM micrographs of the 0.1PZT-0.9PMN ceramics sintered for 4 h at (a) 1200 ^{o}C, (b) 1225 ^{o}C, (c) 1250 ^{o}C, (d) 1275 ^{o}C, (e) 1290 ^{o}C and (f) 1320 ^{o}C.

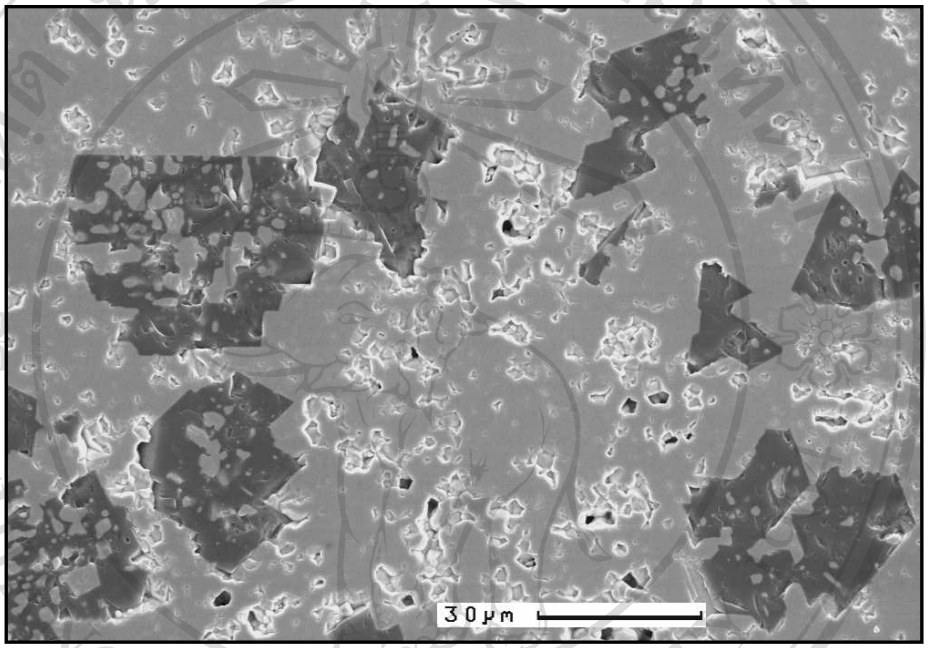

Fig. 6.15 SEM micrograph of polished surface of 0.1PZT-0.9PMN sintered at 1275 ^{o}C for 4 h with heating/cooling rates of 10 ^{o}C/min (darker grains are pyrochlore phases).

6.3 Dielectric Properties

The temperature and frequency dependences of dielectric constant and dissipation factor for the entire range of solid solution *x*PZT-(1-*x*)PMN ceramics are shown in Figs. 6.16-6.21. In general, a relaxor dielectric response similar to that of pure PMN is observed for compositions with higher PMN concentrations. The response changes gradually towards that of a typical normal ferroelectric PZT with increasing *x*. These trends are observed in both the dielectric constant and the dissipation factor behaviours.

The characteristic of dielectric constant and dissipation factor of 0.9PZT-0.1PMN are shown for different sintering temperatures in Fig. 6.16. Phase transitions from ferroelectric to paraelectric state are clearly observed from the peak of dielectric constant. The temperature at which highest value of the dielectric constant is observed corresponds to the Curie temperature. The results also show frequency independent of T_c of samples obtained at different sintering temperatures. These samples exhibit T_c at approximately 350 ^oC which is slightly lower than that of pure PZT (~ 380 ^oC, from section 4.3). This observed T_c is at the same temperature range of the 0.875PZT-0.125PMN ceramics found by Koval et al.[73] They also reported the relaxor behavior but it is not seen here. For this particular composition, the present result reveals a higher T_c than that of thin film prepared using a sol-gel method.[154] The effect of an interfacial layer between the electrode and the film, the small grain size, and the clamping associated with the substrate might be responsible for this lower T_c value.

The very interesting feature in this work is the dielectric constant and dissipation factor response of 0.9PZT-0.1PMN shown in Fig. 6.16(e). The sample shows all the characteristics of a normal ferroelectric material with the highest

dielectric constant of nearly 30000 at 1 kHz. This value is much higher than the highest resported values (~24000) for pure PMN ceramics (*Chapter 5*). For dissipation factor results, it can be seen that low loss level is observed in the range from room temperature to about 200 ^{o}C. This behavior is similar to that of pure PZT but it was only observed in a narrower range, i.e. room temperature to 100 ^{o}C.

Fig. 6.17 is the plot of dielectric constant (measured at 1 kHz) as a function of temperature for 0.9PZT-0.1PMN samples form several sintering temperatures. It can be seen that profiles of dielectric constant variation for all samples are similar even they were sintered at different sintering temperatures. However, the $\varepsilon_{r,\ max}$ are increased with increasing sintering temperature and there is no shifting of the T_c. It is clearly that increasing of $\varepsilon_{r,\ max}$ is associated with development of grain size as observed by SEM micrograph (Fig. 6.10). The 0.7PZT-0.3PMN ceramics exhibit broader peak of the dielectric constant comparing to 0.9PZT-0.1PMN ceramic. This broadening is also varying with the sintering temperature. As sintering temperature increases, the peak becomes narrower.

The temperature dependence of the dielectric constant and the dissipation factor of lead-based perovskite solid solution *x*PZT-(1-*x*)PMN at $0.5 \leq x \leq 0.1$ for different frequencies are shown in Figs. 6.19-6.21. The dielectric constant has a broad maximum ($\varepsilon_{r,max}$) at a temperature T($\varepsilon_{r,max}$) at each frequency. As the frequency increases, the value of T($\varepsilon_{r,max}$) shifts towards higher temperatures. The tan δ also has a broad maximum at a temperature T(tan δ_{max}) slightly lower than T($\varepsilon_{r,max}$). As the frequencies increases, the T(tan δ_{max}) of the compositions at $x = 0.3$ and 0.1 is shifted towards higher temperatures and the area below the tan δ-curve increases. Whilst for *x*

= 0.5, the opposited trend is observed. This observation could be attributed to the effect of different chemical composition, degree of composition fluctuation and also cation-ordering characteristic which has been believed to govern the dielectric dispersion in the transition region.[153]

In addition, it is seen that the increase of PMN/PZT ratio in the (1-*x*)PZT-*x*PMN system increases the fraction of tetragonal phase and enhances the extent of dielectric dispersion and diffuse phase transition around dielectric permittivity peak. The enhanced diffuse phase transition in PZT-PMN system suggests that more 1:1 short-range ordered micro-nanodomains formed [136]. Since the average Zr:Ti ratio in the (1-*x*)PZT-*x*PMN system is 0.52:0.48 (as different from 1:1 for the ordered micro-domains), the enhanced 1:1 short-range ordering of Zr:Ti in the presence of PMN thus expedites the B-site compositional fluctuation occurring on a nanometer scale. This further illustrates that micro-compositional inhomogeneity is responsible for the diffuse phase transition behaviour in the PZT-PMN system. For this type of ordering, because the Zr:Ti and Mg:Nb ratio are 1:1 within the nanometer-sized ordered domains, strong charge effect will result, where the ordered (Zr-rich or Mg-rich) micro-domains will have a net negative charge with respect to the disordered (Ti-rich or Nb-rich) matrix.

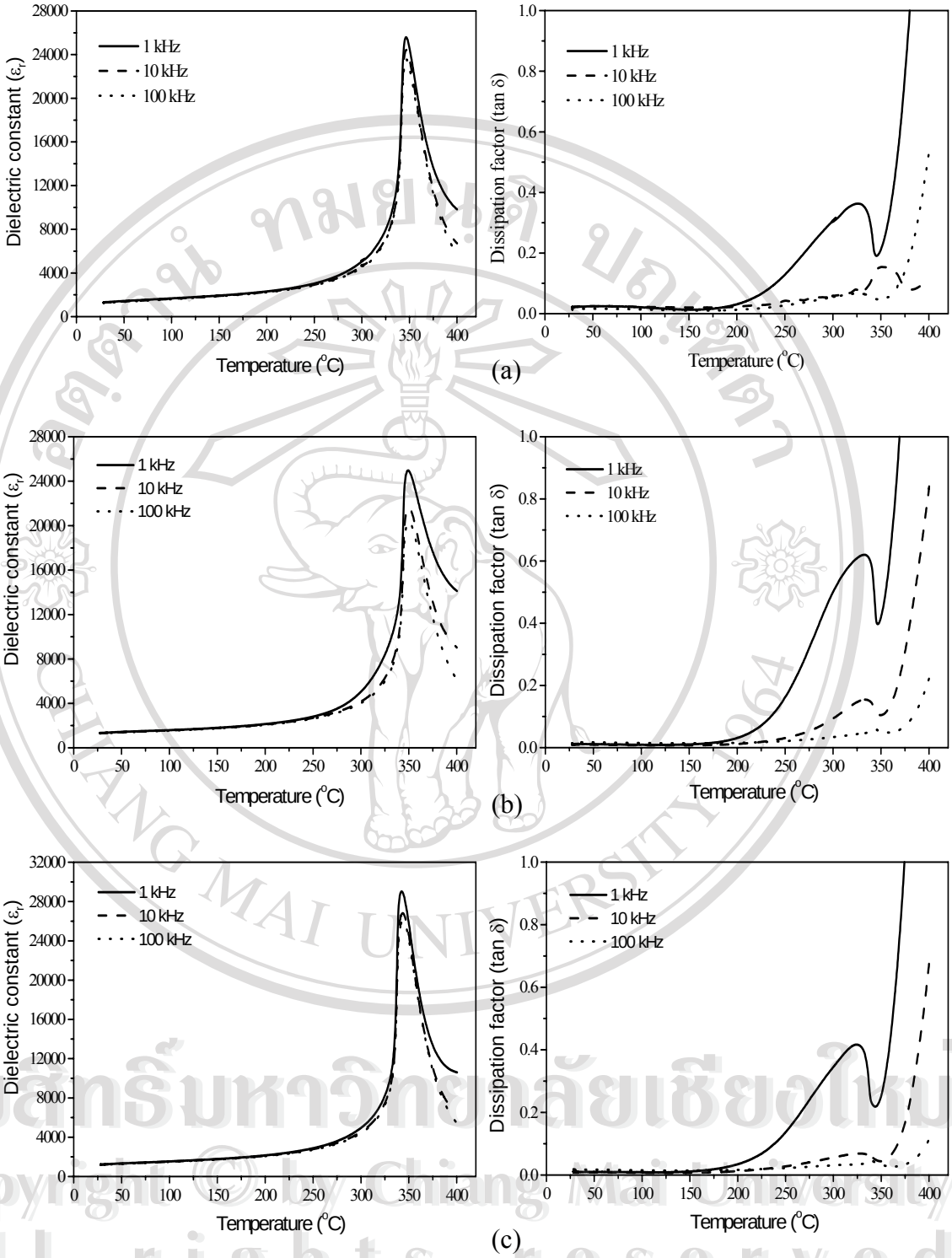

Fig. 6.16 Dielectric constant and dissipation factor as a function of temperature of 0.9PZT-0.1PMN samples sintered at (a) 1200 ^{o}C, (b) 1225 ^{o}C, (c) 1250 ^{o}C, (d) 1275 ^{o}C and (e) 1290 ^{o}C.

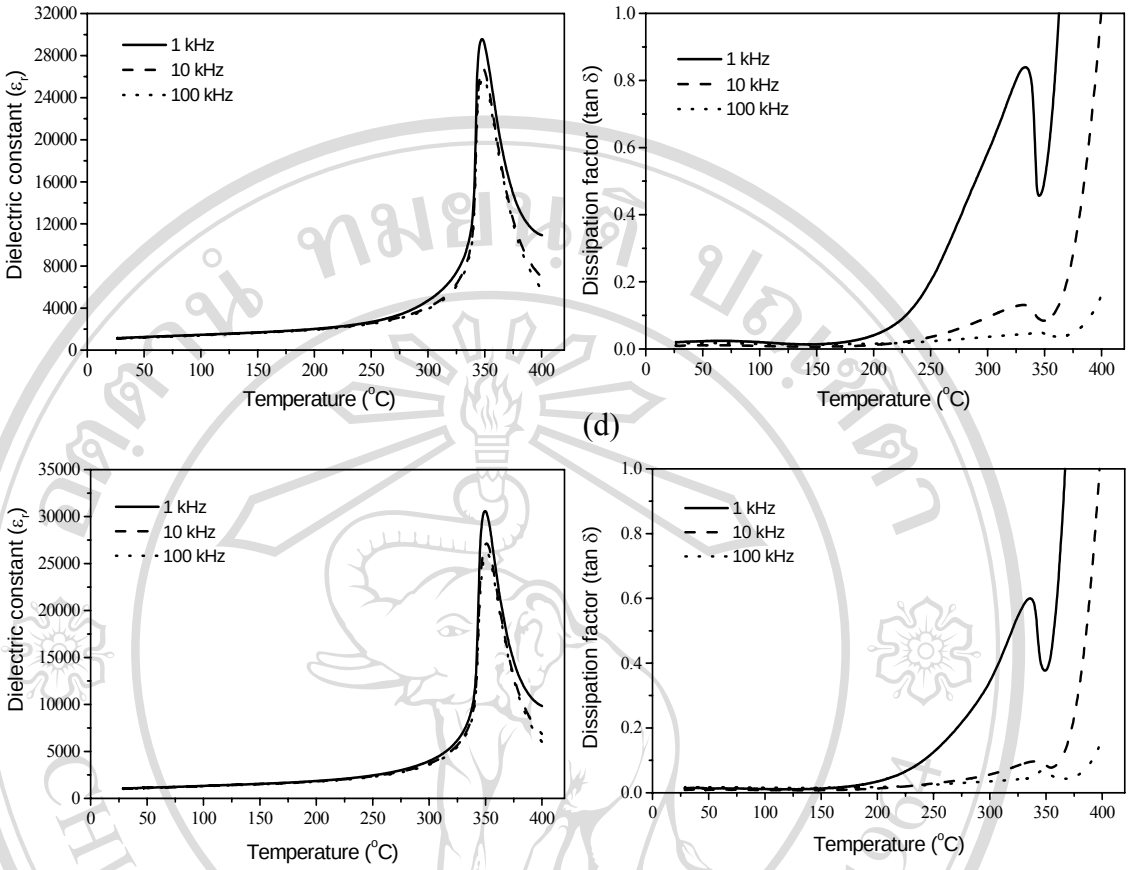

Fig. 6.16 (Continuous)

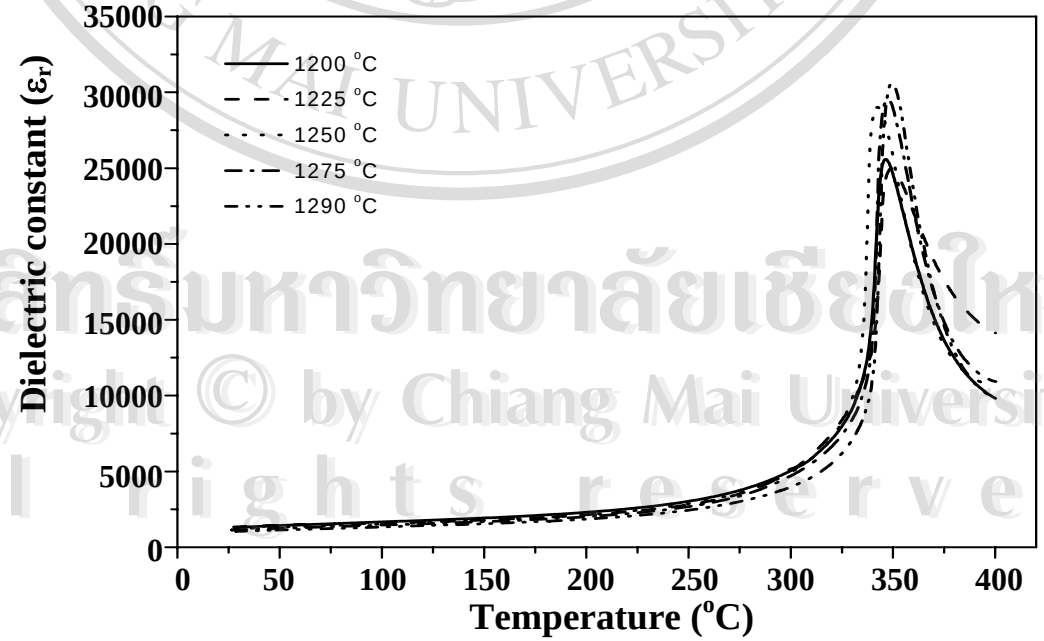

Fig. 6.17 Temperature dependence of dielectric constant of 0.9PZT-0.1PMN ceramics sintered at different sintering temperature (measured at 1 kHz).

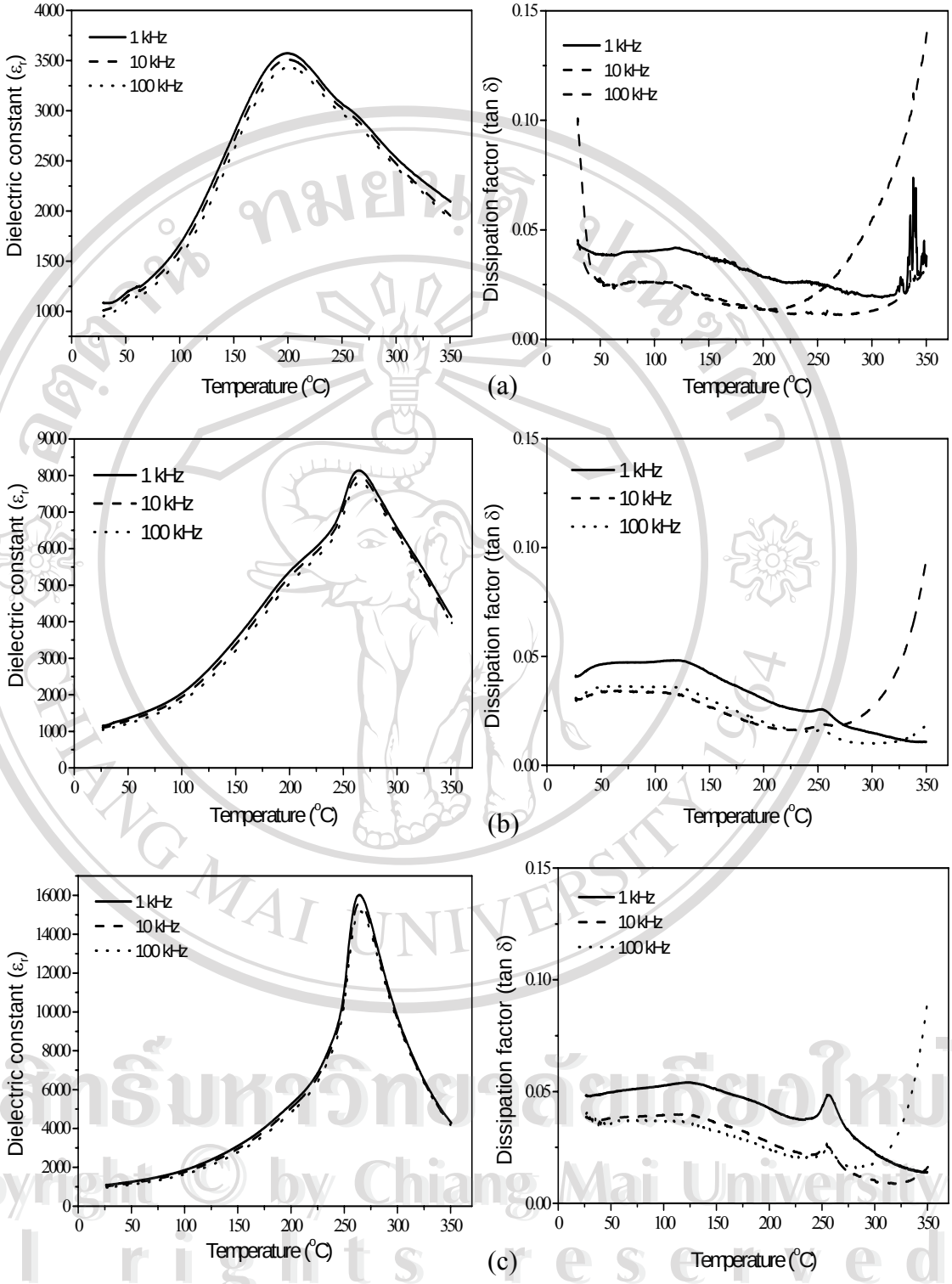

Fig. 6.18 Dielectric constant and dissipation factor as a function of temperature of 0.7PZT-0.3PMN samples sintered at (a) 1225 °C, (b) 1250 °C, (c) 1275 °C, (d) 1290 °C and (e) 1320 °C.

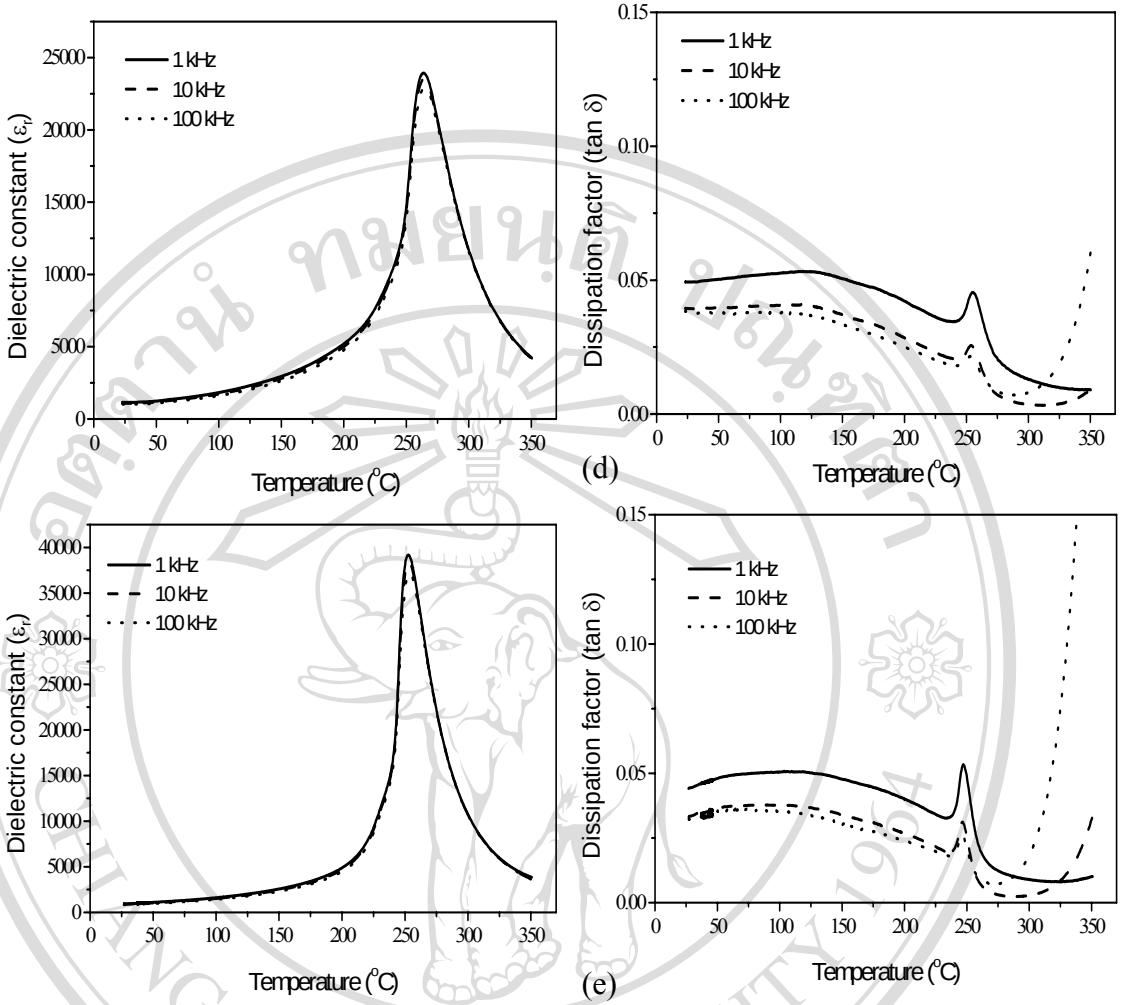

Fig. 6.18 (Continued)

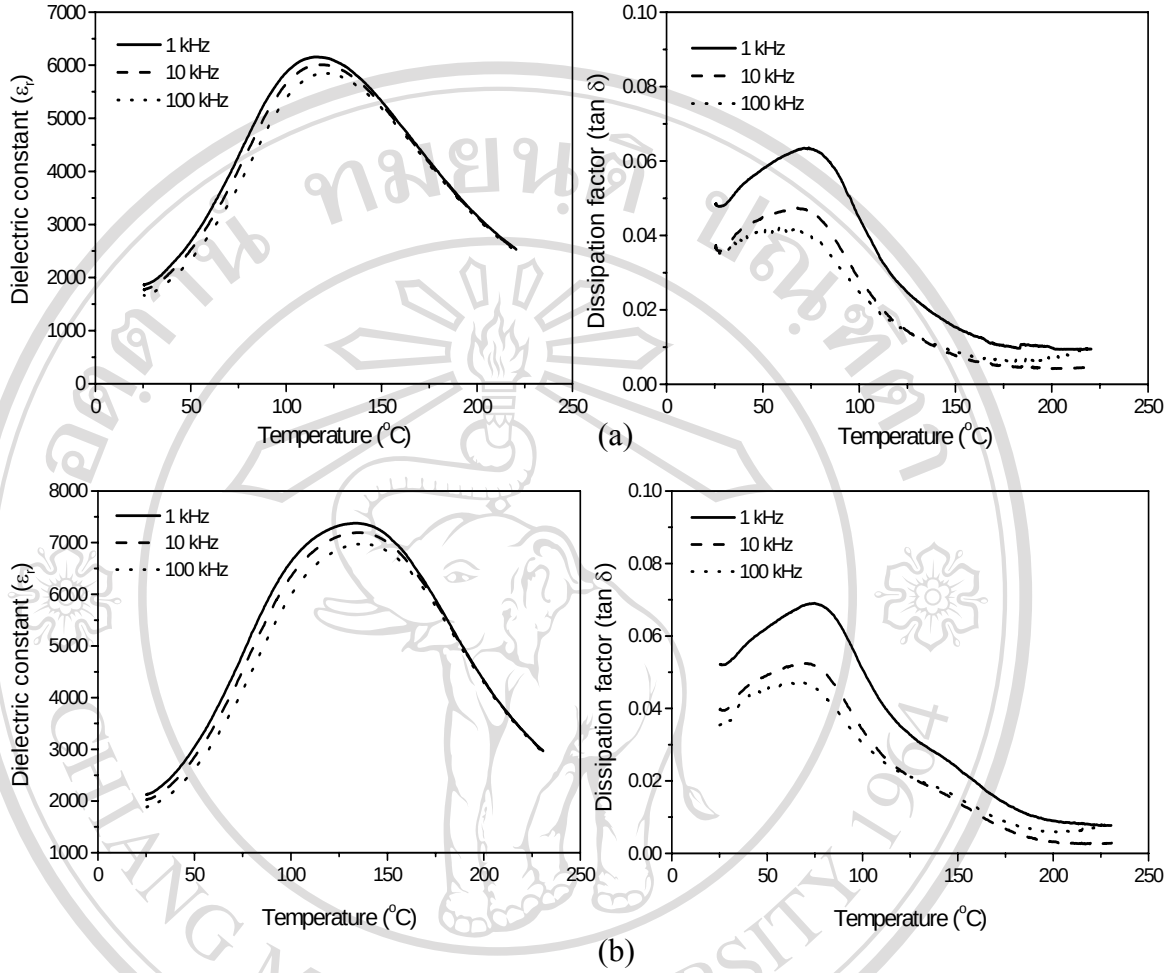

Fig. 6.19 Dielectric constant and dissipation factor as a function of temperature of 0.5PZT-0.5PMN samples sintered at (a) 1225 °C, (b) 1250 °C, (c) 1275 °C, (d) 1290 °C and (e) 1320 °C.

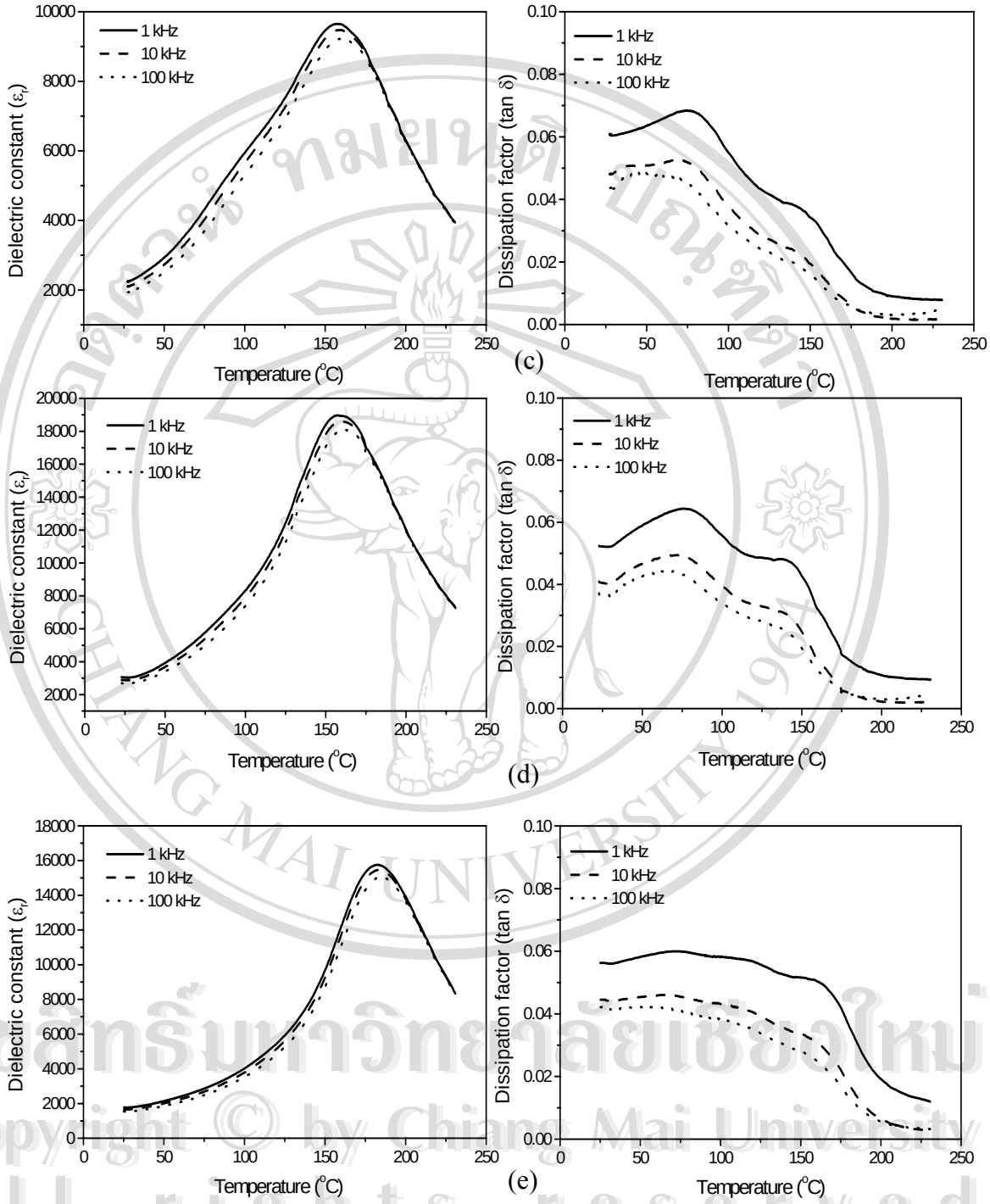

Fig. 6.19 (Continued)

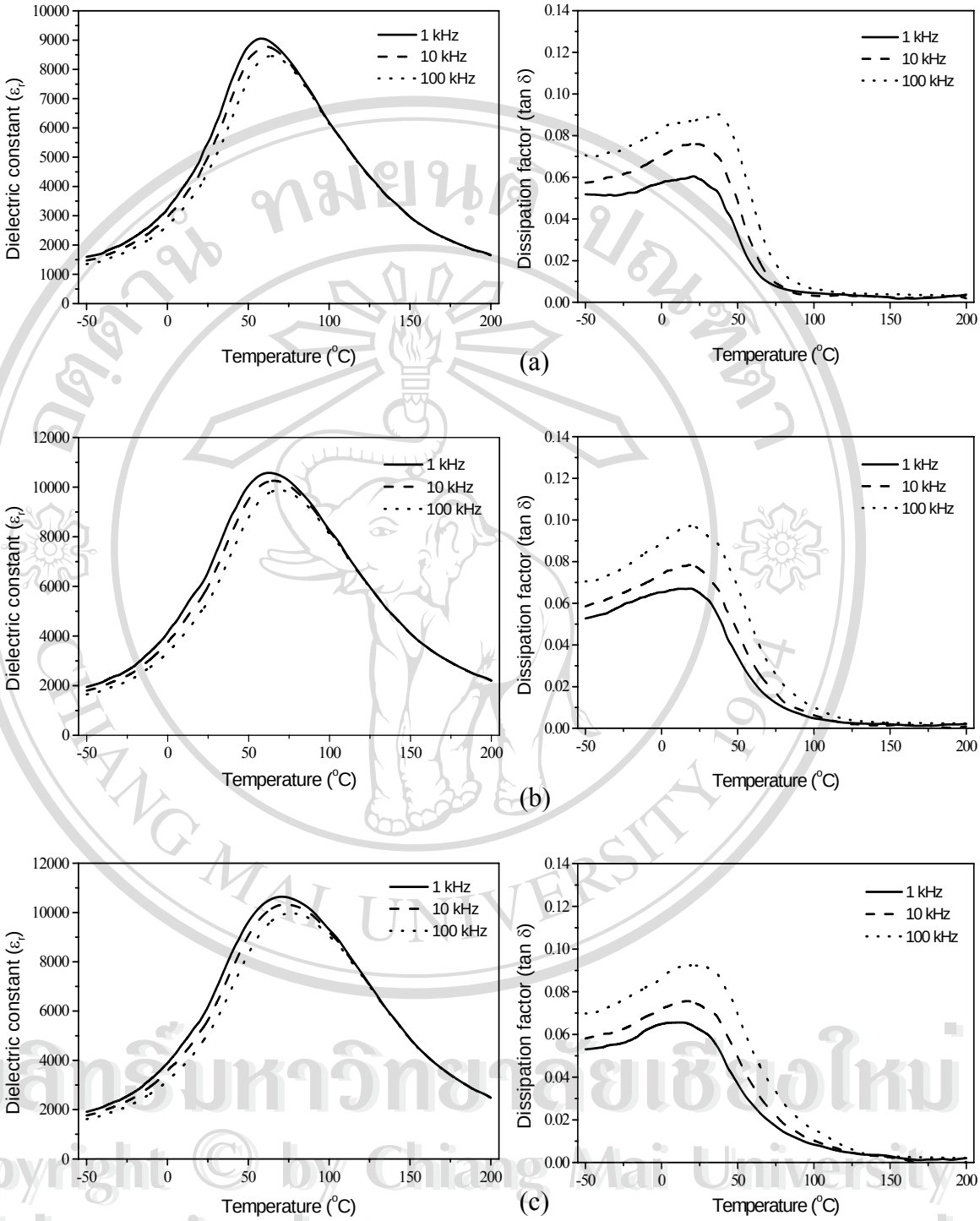

Fig. 6.20 Dielectric constant and dissipation factor as a function of temperature of 0.3PZT-0.7PMN samples sintered at (a) 1200 ^{o}C, (b) 1225 ^{o}C, (c) 1250 ^{o}C, (d) 1275 ^{o}C and (e) 1290 ^{o}C.

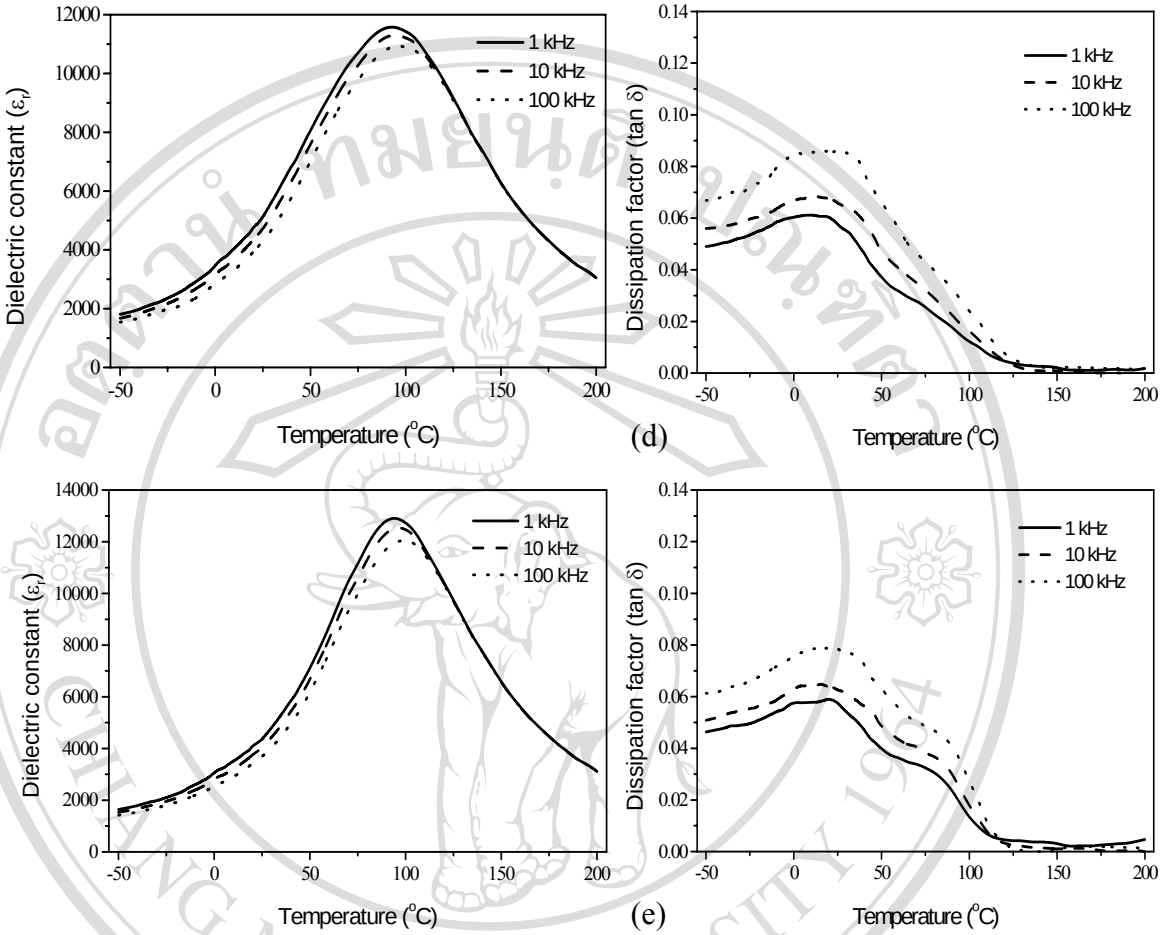

Fig. 6.20 (Continued)

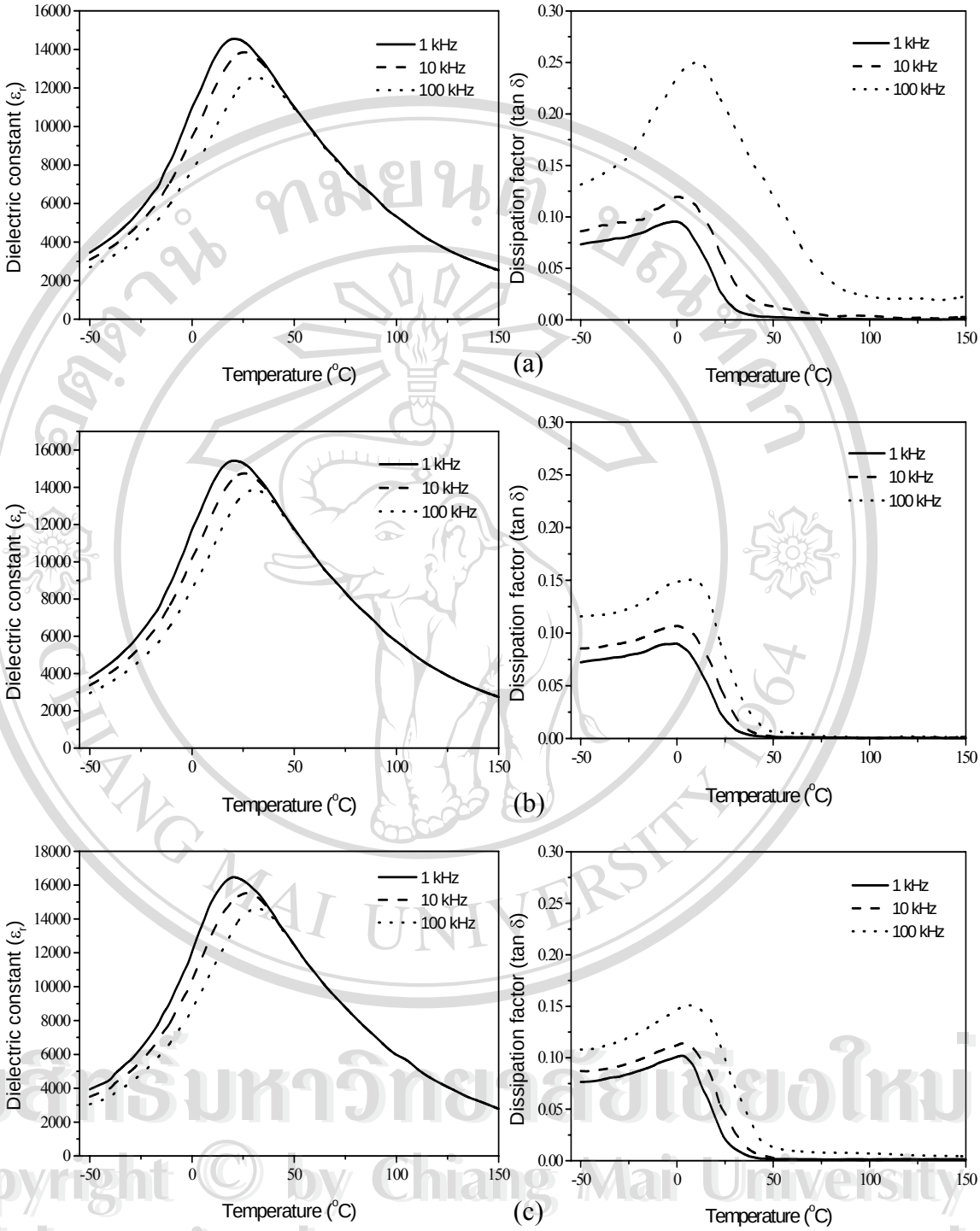

Fig. 6.21 Dielectric constant and dissipation factor as a function of temperature of 0.1PZT-0.9PMN samples sintered at (a) 1200 °C, (b) 1225 °C, (c) 1250 °C and (d) 1275 °C.

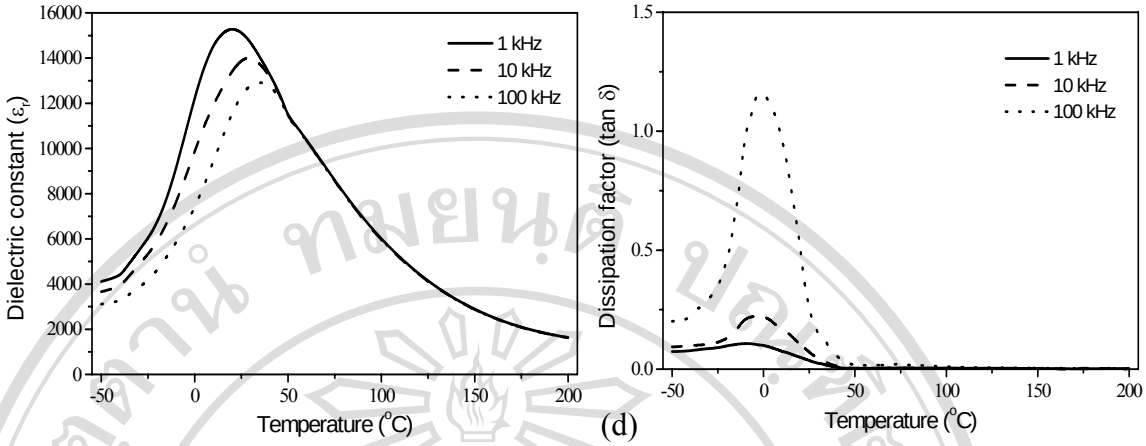

Fig. 6.21 (Continued)

6.4 Microstructure and Electrical Property Relationships

The dielectric properties measurement at room temperature for each compositions at various sintering conditions are summarized in Table 6.4. The observed room temperature dielectric constant as a function of PZT concentration (x) at a frequency of 1 kHz is plotted in Fig. 6.22. As shown, high room temperature dielectric constant was found for compositions near PMN-rich phases. This is probably due to the low Curie point nature of PMN component as also found in PMN-PT system.[155] Above $x = 0.1$, the room temperature dielectric constant decreased with PMN concentration, indicating a chemical composition dependence, as similar to that found in PMN-PT ceramics, which was believed to be due to change of the polar domain region.[155] The dissipation factors at room temperature were found to be similar in all compositions containing higher amounts of PZT ($x > 0.1$). This observation indicates that only a small addition of PZT is sufficient to inhibit macrodomain wall motions and hence less dissipation factors.

Table 6.4 Dielectric properties of *x*PZT-(1-*x*)PMN ceramics taken from data measured at 1 kHz and room temperature (20 ^{o}C).

Sintering temperature	*x* = 0.1		*x* = 0.3		*x* = 0.5		*x* = 0.7		*x* = 0.9	
(^{o}C)	$\varepsilon_{r,RT}$	tan δ	$\varepsilon_{r,RT}$	tan δ	$\varepsilon_{r,RT}$	tan δ	$\varepsilon_{r,RT}$	tan δ	$\varepsilon_{r,RT}$	tan δ
1100	-	-	-	-	-	-	-	-	1201	0.156
1150	2951	0.037	5059	0.050	-	-	-	-	**1354**	**0.034**
1200	2545	0.047	3497	0.073	-	-	-	-	1348	0.019
1225	15488	0.032	**6333**	**0.059**	1937	0.043	913	0.032	1202	0.013
1250	**16171**	**0.034**	5388	0.068	**2241**	**0.038**	**1140**	**0.033**	1119	0.010
1275	12527	0.075	4817	0.050	2032	0.037	1053	0.034	1022	0.016
1290	2951	0.037	4147	0.051	1879	0.036	1042	0.034	/	/
1320	/	/	/	/	1048	0.035	922	0.034	/	/

-: these data were omitted due to highly porous ceramics were obtained.

/: PZT-PMN samples with large concentration of pores at the surface not suitable for measurement.

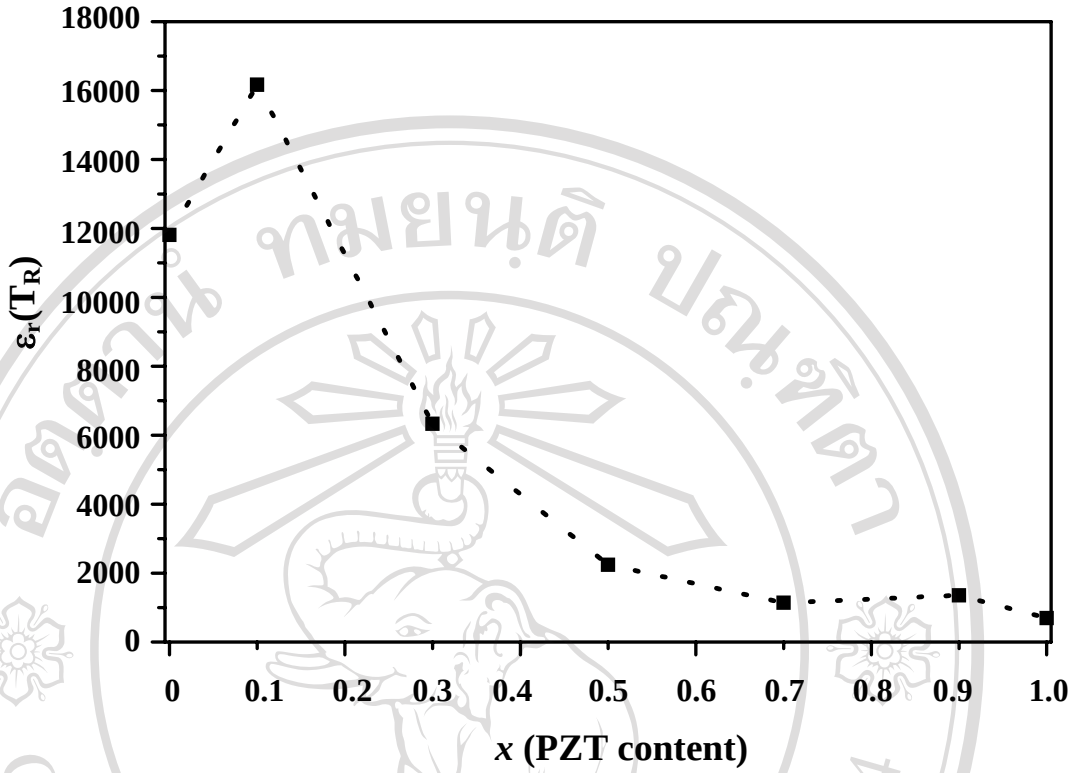

Fig. 6.22 Room temperature dielectric constant of *x*PZT-(1-*x*)PMN ceramics as a function of *x*.

The $\varepsilon_r(T_R)$ and $\varepsilon_{r,max}$ for each *x*PZT-(1-*x*)PMN ceramics are plotted as a function of it average grain size as shown in Figs. 6.23 and 6.24, respectively. In general, it is seen that the effect of grain size on $\varepsilon_r(T_R)$ was found to be quite significant only at $x \leq 0.3$, i.e. the PMN-rich composition. Whilst the $\varepsilon_{r,max}$ values tend to increase with increasing *x* especially for compositions with $x \geq 0.3$. It is to be noted that there is no obvious interpretation of these results, although it is likely to correspond to the effect of PbO volatilization mechanism at high sintering temperature suggested by Kong et al.[152]

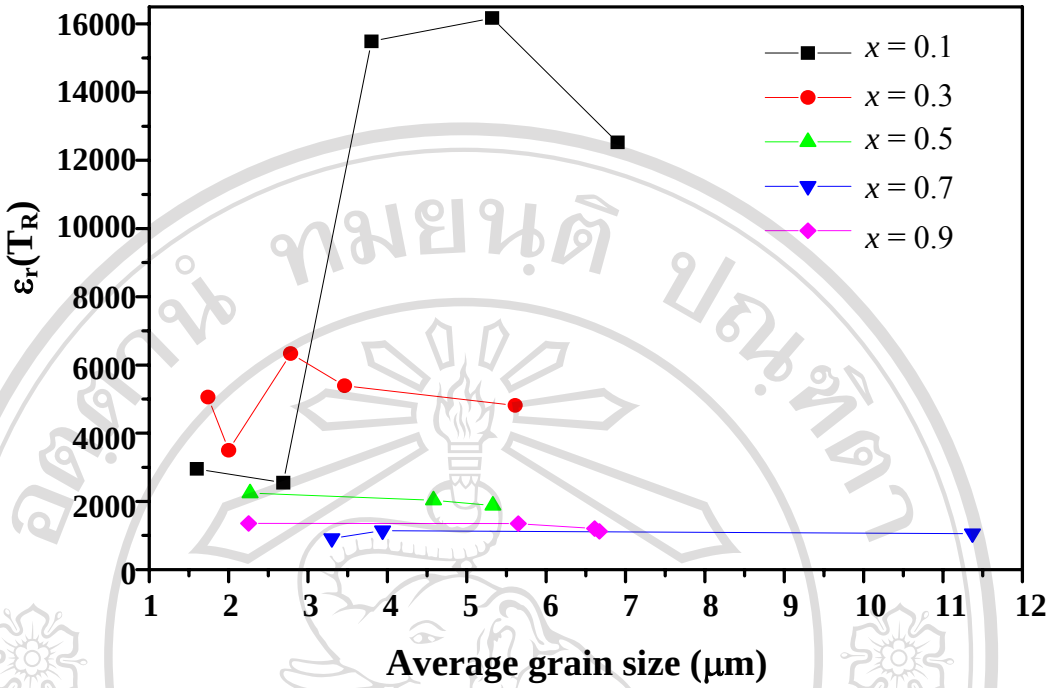

Fig. 6.23 The dielectric constant at room temperature versus average grain size of *x*PZT-(1-*x*)PMN ceramics.

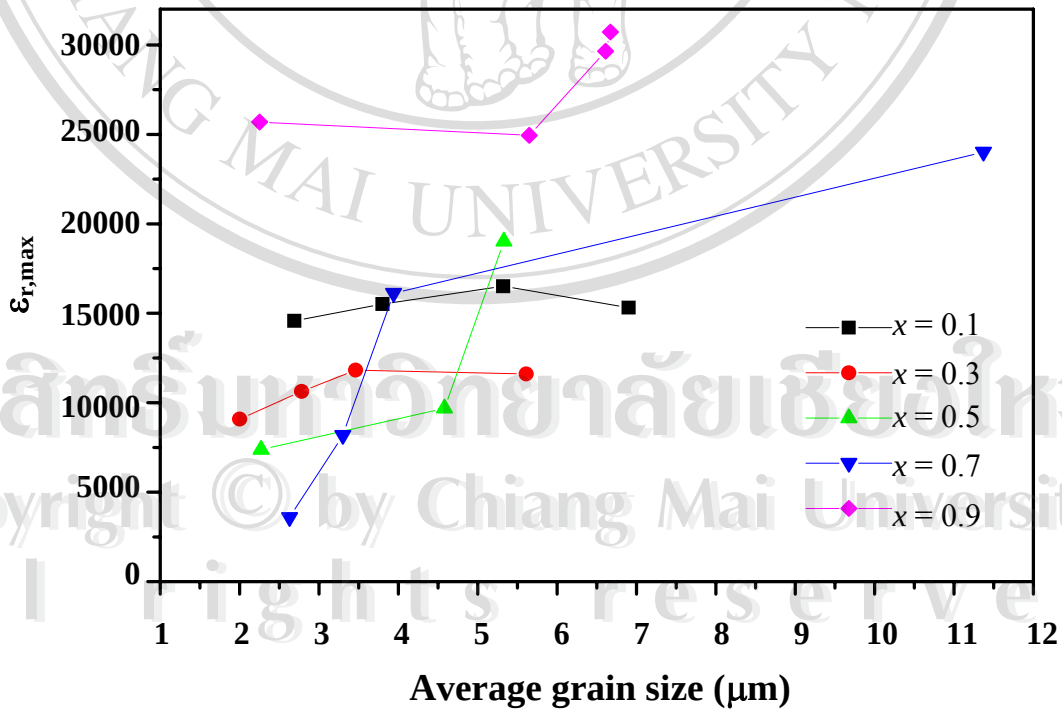

Fig. 6.24 The maximum dielectric constant versus average grain size of *x*PZT-(1-*x*)PMN ceramics.

The variations of the dielectric constant (ε_r) and dissipation factor (tan δ) at 1 kHz as a function of temperature at different compositions are shown in Figs. 6.25 (a) and (b), respectively. The $\varepsilon_{r,max}$ and tan δ_{max} values decrease with increasing *x* until it reaches a minimum at $x = 0.3$ and then increases with increasing *x* until it reaches a maximum at $x = 0.7$ and then decreases with increasing *x* further. The temperatures of both the maximum dielectric constant, $T(\varepsilon_{r,max})$, and dissipation factor, $T(\tan \delta_{max})$, increase with increasing *x* as expected.

The characteristic behaviours of the dielectric constant and of the dissipation factor in two different composition ranges are summarized in the following:

(i) $0.0 \leq x \leq 0.5$, the solid solutions in this composition range behave more or less like pure relaxor PMN. The $\varepsilon_r(T)$ curve near the maximum is broadened, and its broadness increases with increasing *x*. There is discrepancy between $T(\varepsilon_{r,max})$ and $T(\tan \delta_{max})$ and they are both frequency dependent.

(ii) $0.7 \leq x \leq 1.0$, these compositions exhibit relatively sharp maxima and their maximum values are large. Characteristic transition temperatures $T(\varepsilon_{r,max})$ and $T(\tan \delta_{max})$ coincide with each other and both are frequency independent.

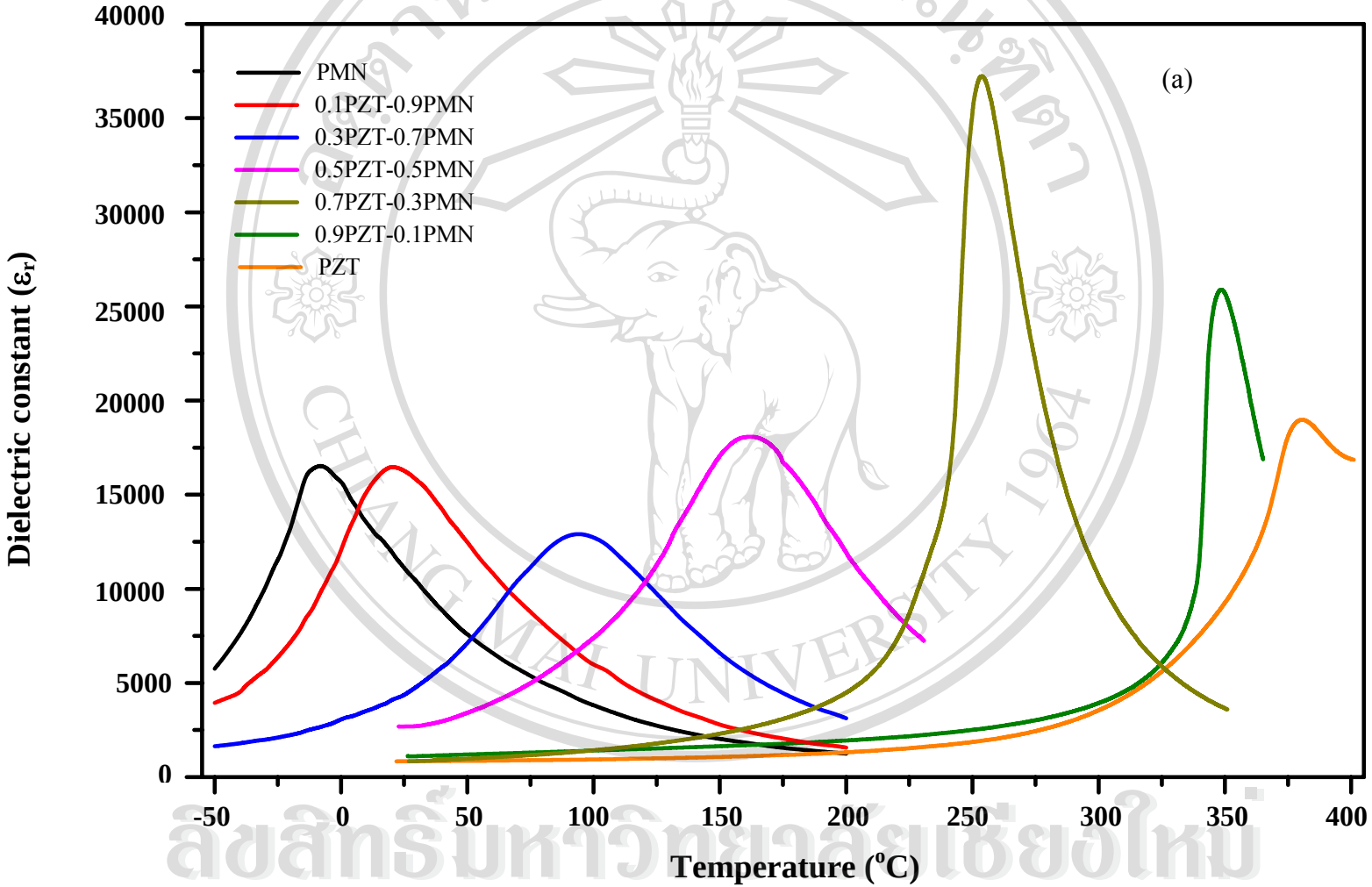

Fig. 6.25 Temperature dependence of (a) the dielectric constant and (b) dissipation factor of *x*PZT-(1-*x*)PMN ceramics.

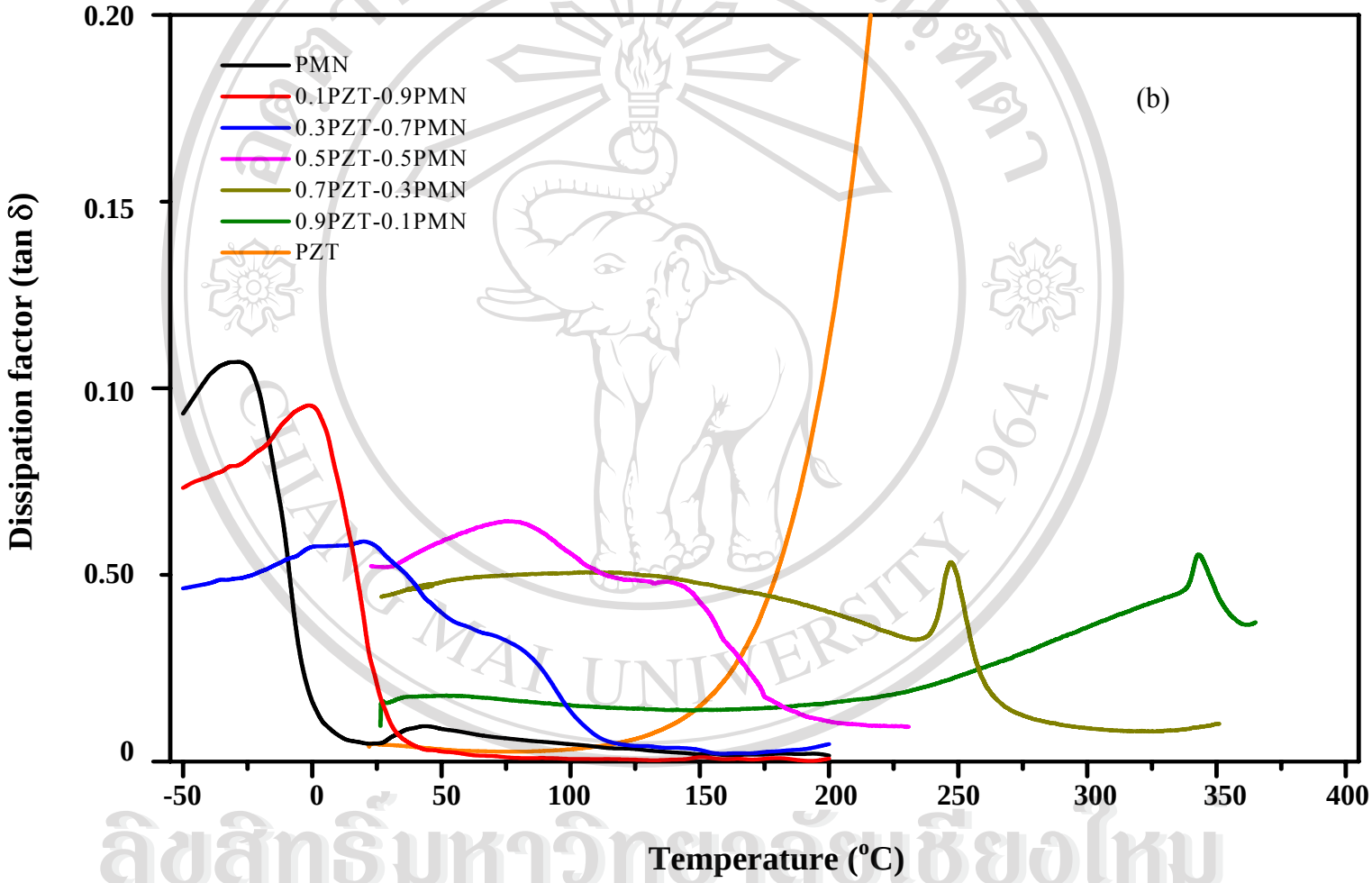

Fig. 6.25 (Continued)

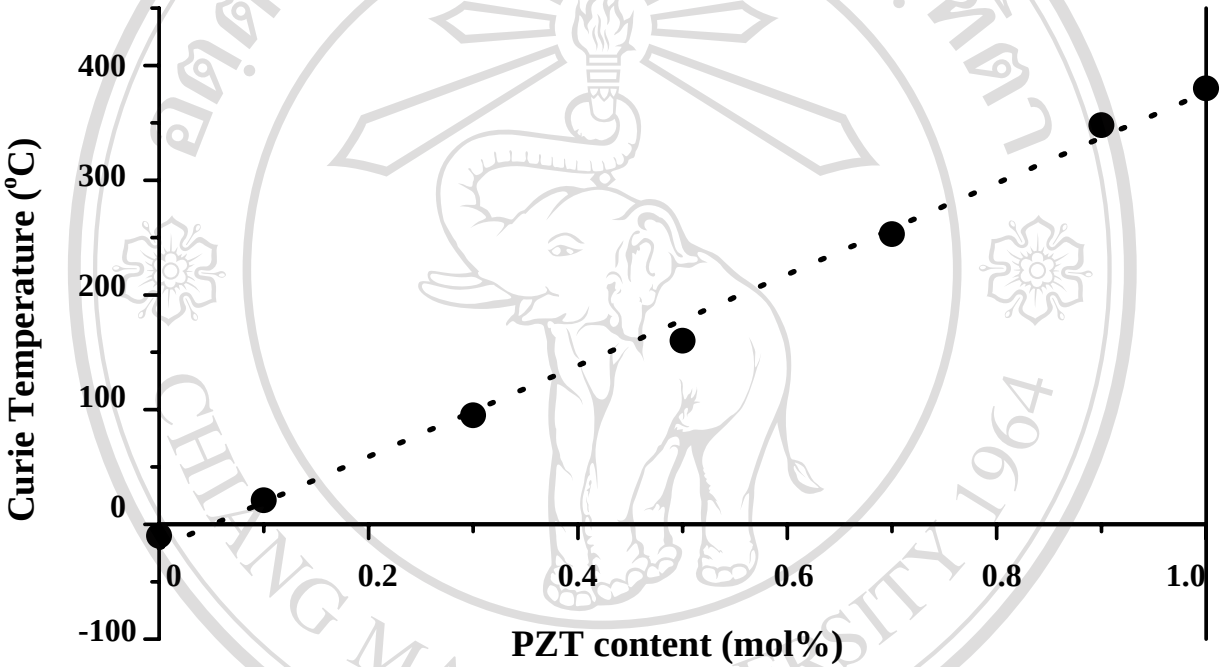

Fig. 6.26 Temperature of dielectric constant maximum of the *x*PZT-(1-*x*)PMN ceramics as a function of PZT concentration.

The temperature of the dielectric constant maximum as a function of PZT concentration (x) at a frequency of 1 kHz for the xPZT-(1-x)PMN ceramics is shown in Fig. 6.26. If one takes T_c as the temperature of a ferroelectric phase transition, then from $T_c(x)$ dependence in Fig. 6.26, it follows that:

i) there is nothing similar to $T_c = A(x - x_c)^{1/2}$ type dependence[137], clearly, there is a linear dependence of T_c on x;

ii) there is no clear phase transition at $0.5 \leq x \leq 0.7$;

iii) for all x, there is a frequency dispersion of the dielectric constant.

The reasons of this unusual dielectric response lay both in the substitution of the foreign ions for the host ions in the A- and B-site simultaneously and in the relaxor nature of PMN, the second-end member of the PZT-PMN solid solutions.

Finally, it is very interesting to note that all relaxor-MPB compositions have T_c in the range of ~150 ^oC-180 ^oC,[141, 155, 156] giving rise to a question of the underlying mechanism which is not fully understood at this time.

The correlation between structure and dielectric properties of $Pb(B_1,B_2)O_3$ type have been previously explained by the onset of internal electric fields whose magnitudes and directions are random. Their origin is related to the tendency of the B_1 and B_2 cations to from 1:1 short range order regions. From the ion radii view point, it is highly probable that Zr^{4+} ions occupy the B-sites of perovskite structure. A possible substitution of Zr^{4+} ions for Nb^{5+} ions would lead to a Mg:Zr order. If ordering of Mg^{2+} and Zr^{4+} with 1:1 ratio is possible in a 0.1PZT-0.9PMN solid solution, this will yields the local B-site valency of 3+. This is also, therefore, electrostatically less favourable than Nb:Zr order. The Nb:Zr is an expected 1:1 order when Zr^{4+} ions substitute for Mg^{2+} ions in the B-site of perovskite structure. Because

of the columbite effect, the most possibility is the substitution of Zr^{4+} for Mg^{2+} rather than Zr^{4+} for Nb^{5+} ions. In addition, the higher favourable of substitution of Zr^{4+} for Mg^{2+} is due to the larger ionic radii of Zr^{4+} ions themselves. Since Zr is tetravalent and Mg is divalent, the Zr behaves as a donor dopant. Therefore, the donor doping with Zr^{4+} ions would be expected to compensate the change imbalance effect resulting from the 1:1 ordering of Mg:Nb. This charge compensation in turn stabilizes the ordered micro-domains, and hence favors an increasing degree of short range ordering.

On the other hand, it is believed that Ti^{4+} ions are not closely involved with the short-range ordering in the $Pb(Mg_{1/3}Nb_{2/3})O_3$ perovskite. By consideration of a possibility of 1:1 ordering of Mg^{2+} and Ti^{4+} ions, this would yields the local B-site vacancy of 3+ but it is electrostatically less favourable than Mg:Nb order. Nb:Ti ordering is also unlikely since this type of 1:1 ordering involves the substitution of small-sized Ti^{4+} ion for relatively large-size Mg^{2+} ion which requires larger strain energy than Mg:Nb ordering. Therefore, the degree of the short-range B-site order is expected to decrease with increasing PZT content. This prediction is consistent with the observation that the degree of diffuse phase transition and dissipation factor decreases with increasing PZT content across the morphotropic phase boundary and agrees very well with other workers.[155, 157, 158]

On the other hand, the diffuse phase transition of almost ferroelectric materials can be explained by so-called Känzig micro-nanoregions[159], each of which has its own transition temperature attributed either to large structural (polarization) or to compositional fluctuations in the vicinity of the transition. Therefore, in the transition process, the sum properties of all the micro-nanoregions will be displayed with a

broad envelope of the transition temperature distribution of individual micro-nanoregions.